5-1-2014

Study of Water Transport Phenomena on Cathode of PEMFCs using Monte Carlo Simulation

Karn Soontrapa
University of Nevada, Las Vegas, karns@unlv.nevada.edu

STUDY OF WATER TRANSPORT PHENOMENA ON CATHODE OF PEMFCS
USING MONTE CARLO SIMULATION

by

Karn Soontrapa

Bachelor of Science in Physics

Chulalongkorn University, Bangkok, Thailand

2004

Master of Engineering in Industrial Engineering

Chulalongkorn University, Bangkok, Thailand

2007

A dissertation submitted in partial fulfillment

of the requirements for the

Doctor of Philosophy - Mechanical Engineering

Department of Mechanical Engineering

Howard R. Hughes College of Engineering

The Graduate College

University of Nevada, Las Vegas

May 2014

We recommend the dissertation prepared under our supervision by

Karn Soontrapa

entitled

Study of Water Transport Phenomena on Cathode of PEMFCS using Monte Carlo Simulation

is approved in partial fulfillment of the requirements for the degree of

Doctor of Philosophy in Engineering - Mechanical Engineering
Department of Mechanical Engineering

Yitung Chen, Ph.D., Committee Chair

William Culbreth, Ph.D., Committee Member

Mohamed Trabia, Ph.D., Committee Member

RF Boehm, Ph.D., Committee Member

Jichun Li, Ph.D., Graduate College Representative

Kathryn Hausbeck Korgan, Ph.D., Interim Dean of the Graduate College

May 2014

ABSTRACT

Study of Water Transport Phenomena on Cathode of PEMFCs using

Monte Carlo Simulation

by

Karn Soontrapa

Dr. Yitung Chen, Examination Committee Chair
Professor of Department of Mechanical Engineering
University of Nevada, Las Vegas

This dissertation deals with the development of a three-dimensional
computational model of water transport phenomena in the cathode catalyst layer (CCL)
of PEMFCs. The catalyst layer in the numerical simulation was developed using the
optimized sphere packing algorithm. The optimization technique named the adaptive
random search technique (ARSET) was employed in this packing algorithm. The
ARSET algorithm will generate the initial location of spheres and allow them to move in
the random direction with the variable moving distance, randomly selected from the
sampling range (α), based on the Lennard-jones potential of the current and new
configuration. The solid fraction values obtained from this developed algorithm are in
the range of 0.631 to 0.6384 while the actual processing time can significantly be reduced
by 8% to 36% based on the number of spheres. The initial random number sampling
range (α) was investigated and the appropriate α value is equal to 0.5.

This numerically developed cathode catalyst layer has been used to simulate the
diffusion processes of protons, in the form of hydronium, and oxygen molecules through
the cathode catalyst layer. The movements of hydroniums and oxygen molecules are

controlled by the random vectors and all of these moves has to obey the Lennard-Jones potential energy constrain. Chemical reaction between these two species will happen when they share the same neighborhood and result in the creation of water molecules. Like hydroniums and oxygen molecules, these newly-formed water molecules also diffuse through the cathode catalyst layer. It is important to investigate and study the distribution of hydronium oxygen molecule and water molecules during the diffusion process in order to understand the lifetime of the cathode catalyst layer. The effect of fuel flow rate on the water distribution has also been studied by varying the hydronium and oxygen molecule input. Based on the results of these simulations, the hydronium: oxygen input ratio of 3:2 has been found to be the best choice for this study.

To study the effect of metal impurity and gas contamination on the cathode catalyst layer, the cathode catalyst layer structure is modified by adding the metal impurities and the gas contamination is introduced with the oxygen input. In this study, gas contamination has very little effect on the electrochemical reaction inside the cathode catalyst layer because this simulation is transient in nature and the percentage of the gas contamination is small, in the range of 0.0005% to 0.0015% for CO and 0.028% to 0.04% for CO_2. Metal impurities seem to have more effect on the performance of PEMFC because they not only change the structure of the developed cathode catalyst layer but also affect the movement of fuel and water product. Aluminum has the worst effect on the cathode catalyst layer structure because it yields the lowest amount of newly form water and the largest amount of trapped water product compared to iron of the same impurity percentage. For the iron impurity, it shows some positive effect on the life time of the cathode catalyst layer. At the 0.75 wt% of iron impurity, the amount of newly

iv

formed water is 6.59% lower than the pure carbon catalyst layer case but the amount of

trapped water product is 11.64% lower than the pure catalyst layer. The lifetime of the

impure cathode catalyst layer is longer than the pure one because the amount of water

that is still trapped inside the pure cathode catalyst layer is higher than that of the impure

one. Even though the impure cathode catalyst layer has a longer lifetime, it sacrifices the

electrical power output because the electrochemical reaction occurrence inside the impure

catalyst layer is lower.

ACKNOWLEDGEMENTS

The first person that I want to express my gratitude is my advisor, Professor Yitung Chen, for his advice and support during the 4 years I have studied at UNLV.

I would like to thank my dissertation committee members: Professor Robert Boehm, Professor William Culbreth, Professor Mohamed Trabia, and Professor Jichun Li, for their time and valuable suggestions. And I also would like to thank my friends for their kind supports.

Finally, I am so grateful that I have both financial and morale support from my mother and brother. I would not have survived this long academic journey without their support.

TABLE OF CONTENT

LIST OF TABLES

LIST OF FIGURES

CHAPTER 1

INTRODUCTION

1.1 Proton Exchange Membrane Fuel Cell

To overcome the increment of fossil fuel price many alternative energy choices

had been introduced and fuel cell is one device among the others that gains some

reputation because of its efficiency to convert chemical energy to electricity [1].

Polymer-electrolyte-membrane or proton exchange membrane fuel cell (PEMFC) is one

of the best fuel cells for future portable power and transportation applications because it

has two unique characteristics which are:

(1) Low-operating temperature: low operating temperature allows PEMFC to
have a shorter start up time compared to another types of fuel cells [1].

(2) High power density: PEMFC utilizes a solid polymer electrolyte which has
the advantages over liquid electrolytes in that the solid electrolyte has a
higher power density and is more resistant to corrosion [1].

Nafion is common material for a polymer electrolyte because of its unique

characteristic which is a very good proton conductor but poor electron conductor and this

characteristic is very critical for PEMFC operation. The catalyst layer, made from

platinum supported on carbon, is deposited onto the membrane. A gas diffusion backing

layer (GDL) which is a porous media made from a carbon cloth is attached to the catalyst

layer to help distributing the reactant to the catalyst layer.

The electrochemical reaction in the PEMFC can be seen in Figure 1.1.
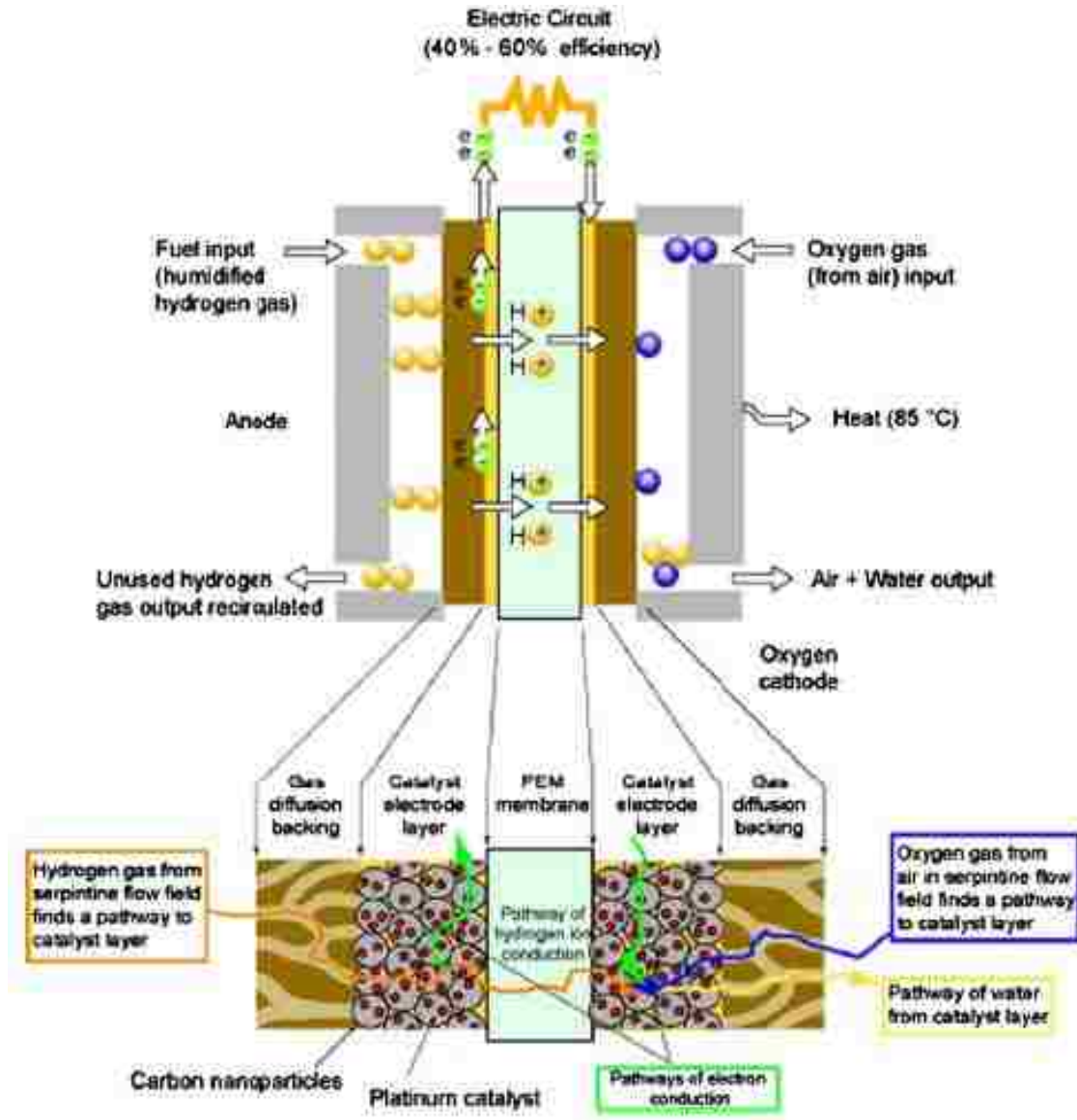
Figure 1.1. Electrochemical reaction in a PEMFC [1].

In Figure 1.1, a humidified hydrogen gas flows into the anode channel and diffuses through the gas diffusion backing layer (GDL) and enters the catalyst layer. At the anode catalyst layer hydrogen separates into protons (H^+) and electrons (e^-) as shown by the equation (1.1).

$$H_2 (g) \rightarrow 2H^+ + 2e^- \tag{1.1}$$

Protons will diffuse through the polymer membrane from the anode catalyst layer to the cathode catalyst layer while electrons will conduct through the external circuit to the cathode catalyst layer. This is the reason why the polymer membrane is a very good proton conductor but poor electron conductor. On the cathode catalyst layer, protons and oxygen will react and form water molecules. The electrochemical reaction at the cathode catalyst layer can be represented by equation (1.2).

$$2H^+ + \frac{1}{2}O_{2(g)} + 2e^- \rightarrow H_2O_{(l)} \tag{1.2}$$

The combination of the electrochemical reaction at the anode and the cathode catalyst layer or the overall chemical reaction is shown by equation (1.3).

$$H_{2(g)} + \frac{1}{2}O_{2(g)} \rightarrow H_2O_{(l)} \tag{1.3}$$
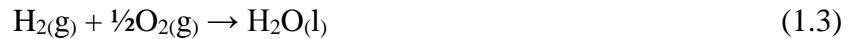
From equation (1.3), it is clear that water is produced at the cathode catalyst layer so that the water concentration at the cathode side is higher than that on the anode side. This product of water can lead to the one of the major losses in PEMFC which is called mass transport loss or concentration loss. As water molecules start to accumulate in the catalyst layer, they will block the movement of protons and oxygen molecules which will dramatically reduce the performance of fuel cells.

Losses in PEMFC can be divided into three categories as follows:

(1) Activation loss: This loss is the result of the slowness of the reaction taking place on the surface of the electrodes. In order to drive the electrochemical reaction that generates the electron, some proportion of the voltage generated is lost because energy is needed to overcome the potential barrier.

(2) Ohmic loss: This is a voltage drop due to the resistance to the flow of protons through the polymer membrane and the flow of electrons through the external circuit.

(3) Mass transport loss or concentration loss: This loss is due to the change in concentration of the reactants at the surface of the electrodes as the fuel is used. As water molecules start to build up at the cathode catalyst layer, less oxygen can flow into the cathode catalyst layer and this will lead to the reactant-starved condition.

Losses in PEMFC can be depicted by the I-V curve in Figure 1.2.
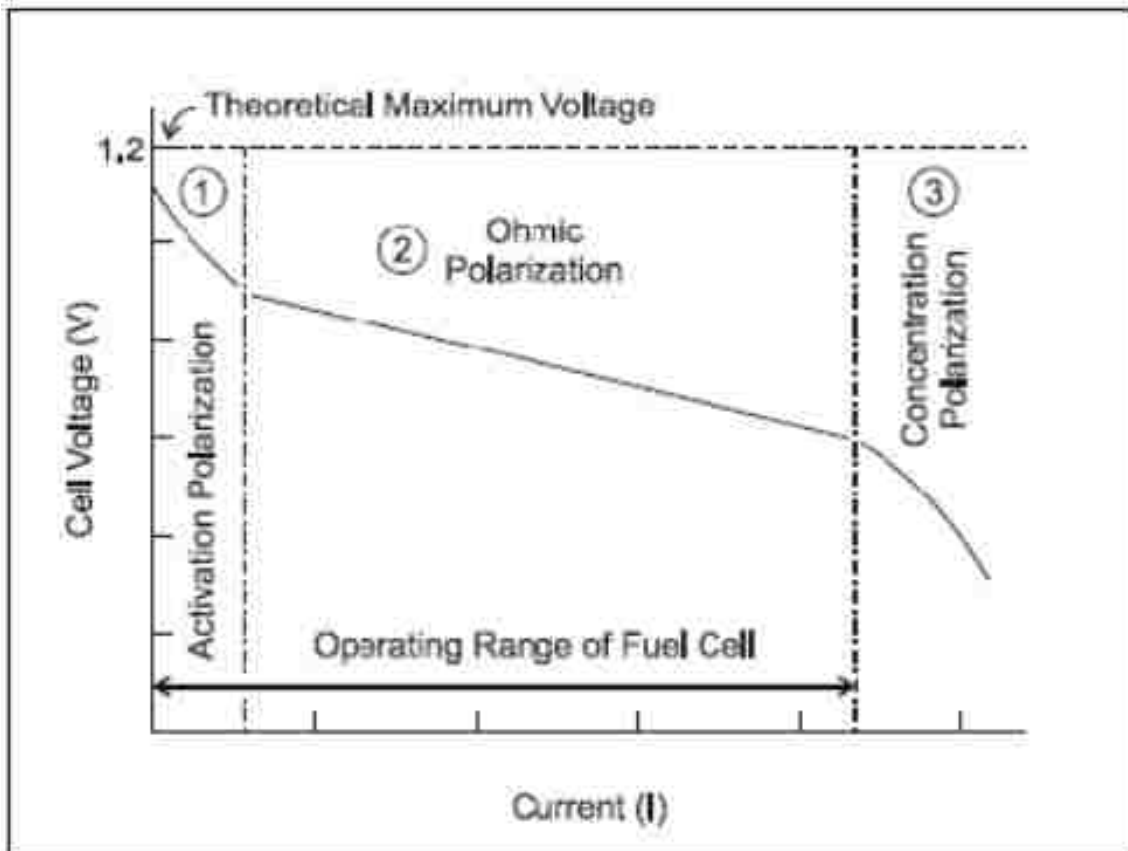
Figure 1.2. I-V curve of a fuel cell showing the individual losses [2].

From Figure 1.2, the theoretical maximum voltage of the PEMFC at the ideal

working condition, 25°C and 1 atm, is equal to 1.23 V but the voltage loss will keep on

going when we allow PEMFC to continuously operate. It is clear that concentration loss

is the major loss in PEMFC. So, the effective way to manage this loss is very important

for the performance for PEMFC. Liquid water management at the cathode side of the

PEMFC is a one effective way to decrease the concentration loss. Excess product water

needs to be expelled from fuel cell catalyst layer in order to keep these fuel cells working

at their optimum level.

<h3 style="text-align:center">1.2 Water Management in PEMFC</h3>

Scholars have proposed many effective ways to manage the liquid water at the

cathode catalyst layer which will be described in this section.

1.2.1 Mathematic Model

Nguyen and White [3] presented a two-dimensional model across the membrane

and along the flow channel of a PEM fuel cell. They modeled the variation in current

density, water transport, stream temperatures and pressure along the channel. They also

modeled the effect of varying anode inlet humidity. However, they ignored the transport

processes in the gas-diffusion layers and the catalyst layers.

Huang et al. [4] presented a two-dimensional water and thermal management

model. In this analysis, they included multiple parameter such as pressure effect,

pressure drop, open circuit voltage dependence on pressure and stack temperature, and

membrane conductivity dependence on anode and cathode side. Results from this model

showed that humidity has a significant effect on the performance of PEMFC especially

on the anode side. While increasing the temperature and pressure, with in a specific range, can increase the performance of PEMFC.

Weber and Newman [5] had developed a non-isothermal one-dimensional model for PEMFC. The temperature gradient between the fuel cell sandwiches can cause a heat-pipe effect which make a liquid water to evaporate and moves toward the gas channel. This water steam will condense and block the movement of reactant-gas which leads to PEMFC's concentration loss. To prevent this phenomenon, temperature inside the PEMFC should be in a certain level because this high temperatures can increase the kinetics and mass transport inside the fuel cell. Another results of this simulation also showed that 65°C and 1 bar is the optimum operating temperature and pressure for PEMFC while the heat removal of 20 W/cm^2 is needed to maintain the best performance.

Dannenberg et al. [6] had developed a two-dimensional model which can simulated heat and mass transfer inside the flow channel of PEMFC. The results from this model showed that PEMFC performed best in the isothermal state and the oxygen depletion or concentration loss can be prevented by adding a well humidified reactant gases. Another results from this work showed that the operating temperature of 80ºC can decrease the ohmic loss in PEMFC.

Fronk et al. [7] addressed several issues regarding PEM fuel cell systems for transportation applications. They highlighted the importance of thermal management while trying to maximize the performance of these systems. The issue of water recovery in the stack and the condenser was discussed. Variation of water and thermal management parasitic loads with variation in the cathode pressure was also investigated in this study.

Geyer and Ahluwalia [8] developed a computer simulation tool which can be used for fuel cell system design and analysis. Their PEM fuel cell model is primarily a curve fit where the voltage is modeled as a function of current, cell temperature and the partial pressure of oxygen at the cathode inlet. They did not model the water transport processes inside the fuel cell and hence, did not take into account variable membrane hydration. They claimed to be able to dynamically model the variation in stack temperature. They employed fundamental models for their condenser and heat exchangers and also had detailed pump models that model the energy consumption of the pumps.

For a unified water transport, Um and Wang [9] developed a model within the single-domain CFCD (computational fuel cell dynamics) framework with the aid of the equilibrium water uptake curve in the membrane phase. They used this to elucidate water management in three-dimensional fuel cells with dry-to-low humidified inlet gases after its validation against available experimental data for dry oxidant and fuel streams.

Shan and Choe [10] proposed a new model constructed upon the layers of a cell, taking into account the following factors: (1) dynamics in temperature gradient across the fuel cell; (2) dynamics in water concentration redistribution in the membrane; (3) dynamics in proton concentration in the cathode catalyst layer; (4) dynamics in reactant concentration redistribution in the cathode GDL.

Haddad et al. [11] developed a dynamical model considering the influence of gas consumption and humidification rates on water diffusion and membrane humidity. With the aid of the dynamical model, an appropriate control of the water content can be built to improving the electrical efficiency and minimizing power losses.

Serincan and Yesilyurt [12] developed a two-dimensional transient single-phase CFD model, incorporating water transport in the membrane and the flow and transport of species in porous gas diffusion electrodes. They used this to study the effect of step changes in cell voltage, cathode air pressure, and relative humidity during start-ups and failures of auxiliary components, such as the loss of pressure in the case of compressor or manifold malfunctions and the loss of humidity in the case of a humidifier malfunction.

Le and Zhou [13] reported a general model specially focused on the liquid water management. They developed a three-dimensional unsteady model with detailed thermo-electrochemistry, multi species and two-phase effects with the interface tracking by using the volume-of-fluid (VOF) method which was implemented into the computational fluid dynamic (CFD) software package FLUENT.

Wang and Wang [14] developed a three-dimensional transient model to study the transient dynamics of a PEMFC. They further performed numerical simulations for a single channel PEMFC undergoing a step increase in current density.

Shimpalee et al. [15] performed three-dimensional CFD simulations of a PEM fuel cell to investigate the effect of GDL flooding on fuel cell performance. The results show that increasing the degree of water flooding as it may occur in untreated GDL, reduces the effective diffusivity of gases dramatically, which in turn increases the concentration and surface overpotentials, and the fuel cell performance is decreased significantly.

Paquin and Fréchette [16] developed a simple one-dimensional model to analyze water management in an air breathing small PEMFC. The results show that decreasing

the ratio between thermal and mass transport resistance under a certain conditions leads to flooding problems while increasing this ratio leads to dry-out of the polymer electrolyte membrane in air breathing PEMFC.

Meng and Wang [17] predicted water flooding inside a PEMFC and the liquid water effects in the cell performance. They affirmed that when the current density is beyond a certain value, too much water will be produced at the cathode and the gas will be saturated by water vapor, then the phase of water vapor begins to change into a liquid phase resulting in cathode flooding. Furthermore, when the current density is greater than 1.4 A cm^{-2}, at the condition of relative humidity equals to 100% for both cathode and anode, water flooding will happen in the cathode, which will be in the case of severe flooding when the water activity (p_w / p_w^{sat}) is in excess of 3.

Lin et al. [18] developed a two-phase, one-dimensional steady-state, isothermal model of a fuel cell region consisting of the catalyst and gas diffusion layers to investigate the effect of water flooding in the gas diffusion layer and catalyst layer of the cathode on the overall cell performance. The simulation results confirmed that the water-flooding situation in the catalyst layer is more severe than that in the gas diffusion backing layer since water is first produced in the catalyst layer.

Liu et al. [19] studied membrane hydration and electrode flooding by developing a two-dimensional partial flooding model in which the pore size distributions are assigned for the hydrophobic and hydrophilic pores of the GDL. The liquid water produced is considered to condense in hydrophilic and hydrophobic pores in sequence if the water vapor pressure is greater than the capillary condensation pressure. In addition, a GDL including a microporous layer (MPL) with a linear porosity is one of the very

effective ways for liquid water draining from catalyst layer into the gas channel when the total thickness of the GDL and MPL is kept constant and the MPL is thinned to 3 μm.

Zhu et al. [20] investigated the dynamic behavior of liquid water entering a PEMFC channel through a GDL pore by performing two-dimensional, transient simulations employing the VOF method. The simulation results show that the height of the channel as well as the width of the pore have significant impacts on the deformation and detachment of the water droplet, and the coalescence of two water droplets can accelerate the deformation rate and motion of the droplets in the micro channel. Furthermore, they simulated the processes of water droplet emergence, growth, deformation and detachment by transient three-dimensional two-phase flow model and found that the wettability of the micro channel surface has a major impact on the dynamics of the water droplet, with a droplet splitting more readily and convecting rapidly on a hydrophobic surface, while for a hydrophilic surface there is a tendency for spreading and film flow formation.

1.2.2 Experimental Data

Fouquet et al. [21] monitored flooding and drying out of a PEM fuel cell using a model-based approach coupled with ac impedance measurements. They found that a cell flooding occurs in two steps: first, accumulation of liquid water inside the GDL while cell voltage drops quite slowly and, after several minutes, the droplets aggregate and block the gas channels, impeding reactants' diffusion to the catalyst sites and inducing in turn a rapid cell voltage drop.

He et al. [22] employed an electrode flooding monitoring device to investigate the correlation between the fuel-cell performance and the liquid water saturation level in the gas diffusion backing layers, the effects of various operating parameters, and the dynamics and hysteresis behavior of liquid water in the gas diffusion backing layers. The results confirmed that the hysteresis behavior of fuel-cell performance during water imbibition and drainage cycle is attributed to the difference in water-removal rate by capillary force and the difference in membrane conductivity.

Natarajan and Nguyen [23] used a segmented electrode/current collector setup to examine the effect of oxygen flow rate, anode sparger temperature, and hydrogen starvation on the spatial and temporal distribution of local current densities along a single gas channel in a PEM fuel cell. They found that when the water removal rate was not sufficient electrode flooding occurred in segments that were farthest from the gas inlet. Once the liquid water fills up the majority of the pores in an electrode, the continuity of the gas phase within the electrode is severely compromised and the sustainable current density will be in the order of a few tens of mA/cm^2 as the limiting currents observed in their experiments.

Kimball et al. [24] examined the process of flooding with a single-channel fuel cell that permits direct observation of liquid water motion. As product water flows through the largest pores in the hydrophobic GDL, drops detach from the surface, aggregate, and form slugs. Flooding in PEMFCs occurs when liquid water slugs accumulate in the gas flow channel, inhibiting reactant transport. They affirmed that flooding is not the result of capillary condensation in the GDL, but rather liquid blocking oxygen transport across the gas/GDL interface.

Although water flooding in PEMFC has been extensively studied, they all focus on the water flooding problems at the gas flow channels. Very few of these studies have reported the new approach in solving water flooding that happens at the cathode catalyst layer. Even though, the cathode catalyst layer is the first area that will be affected by the water flooding problem.

This excess product water must be repelled out of cathode catalyst layer otherwise it will block the movement of protons and oxygen molecules which will dramatically reduce the performance of fuel cells. To improve the performance of PEMFCs, appropriate water management strategies should be studied and one of the best ways to develop these water management strategies is to investigate how water is formed and moved out of the cathode catalyst layer which means this study will be at the atomic level.

To simulate the electrochemical reaction at the atomic level, the appropriate technique must be utilized and the Monte Carlo technique is one of the most famous techniques that can deal with the proposed study.

1.3 Monte Carlo Technique

The Monte Carlo technique is a stochastic algorithm that utilizes a random sequence of number to obtain numerical results. In this dissertation, the Monte Carlo technique is used to simulate the cathode catalyst layer and track the movement of reactants and product water. The Monte Carlo technique is very useful because it can simulate the system with many degrees of freedom and it can deal with the uncertainty input.

The self-developed computer code that used in this dissertation is written in Mathematica which is one of the most powerful global computation languages. Mathematica was chosen because of its flexibility to be modified and its powerful graphic output. Mathematica code, line by line, is easy to read and follow compared to other programing language tools such as Matlab.

1.4 Dissertation Purpose

This dissertation offers a new approach to study the transport phenomena of protons, oxygen molecules and water molecules in PEMFC. With modeling via the Monte Carlo simulation, the behaviors of reactant and product water on the cathode catalyst layer can be obtained, which can help to study the life time of the cathode catalyst layer. In addition, this simulation can also suggest the effect of the contamination in the cathode catalyst layer which can lead to the developments of a new catalyst for PEMFC. The rest of this dissertation is arranged as follows:

• Chapter 2 shows the optimized approach to create the cathode catalyst layer.

• Chapter 3 describes the modeling result of the chemical reaction in cathode catalyst layer.

• Chapter 4 discusses about the effect of the cathode catalyst layer structure on the water distribution.

• Chapter 5 concludes the dissertation.

CHAPTER 2

POROUS MEDIA STRUCTURE CREATION USING SPHERES PACKING

ALGORITHM

2.1 Introduction

Water transport is one of the most critical issues for PEMFCs. Excess product water needs to be expelled from fuel cell catalyst layer in order to keep these fuel cells working at their optimum level. The excess product water will diffuse out of the catalyst layers through gas diffusion layers which were made of porous media, so the best approach to understand the transport phenomena inside PEMFCs is to first understand the porous media structure which will allow us to gain more knowledge how to improve the water management in PEMFCs. Sphere packing is a way to create the porous media structure and there are many publications about the creation of porous media structure using sphere packing approach.

Hermann et al. [25] simulated a nano-porous dielectric material with low dielectric constant (k) value by randomly packed hard spheres. The spheres and the space between them represent the pores and the solid material of the insulator. They claimed that a local maximum of 70% porosity is obtained for a power-law pore size distribution with exponent -3.3. And the elastic constants of their models were calculated for the isotropic case in the composite sphere assemblage approach. From their packing result, the Young's modulus and the bulk and shear modulus are presented for the range of porosity up to 70%.

Scott and Kilgour [26] proposed that models of randomly packed spheres which exhibit some properties of simple liquids in that their radial distribution function and packing density are similar. They conducted experiments for both random loose packing and random close packing with 1/8 in. plexi-glass, nylon and steel balls in air and also with steel balls immersed in oil. A series of measurements for random loose packing and for random close packing, with help of a mechanical vibrator, were made. The obtained packing density for random loose packing was 0.60 and for random close packing was 0.63.

Berg et al. [27] studied the packing of spheres experimentally with approximately 5,000 ball bearings of 1/8-inch diameter. The ball bearings were poured into a plexiglass cylindrical container which is 63 mm in diameter. After that water was poured into the container and then frozen. The ice block was taken out of the container and structure was examined as the thawing of the ice progressed from the boundary inwards. By weighing the balls and measuring the height to which they filled the container determined the density, which varied from 0.586 to 0.592. The container was then placed on a shaker and treated for certain period of time. Three different types of shakers were used, which yielded densities of 0.615, 0.612 and 0.614. Sphere packing configuration depends very much on the mode of shaking; one-dimensional shaking gives irregular random packing. On the other hand, three-dimensional shaking gives an almost perfect hexagonal close packed structure, with packing density of 74%. All the reported experiments were one-dimensional shaking, which gave a random packing of 61%.

Powell [28] generated a structure of randomly packed equal size spheres using computer simulation. The study was aimed at determining the nearest neighbors in the

assembly. He claimed that the properties of particulate assemblies such as the structural properties of powders or electrical conductivity depend on the number and distribution of contacts of each particle, hence, the number of nearest neighbors is of particular interest in the range of r = 1.0 to 1.1 sphere diameter since this determines the number of actual touching contacts and the number of near contacts. He determined the density of random close packing of the computer-generated assembly to be 0.636.

Jodrey and Tory [29] had developed an algorithm which generates a random close packing of equal spheres from a random distribution of points. Each point is the center of an inner and an outer sphere. Their algorithm eliminates overlaps among outer spheres while slowly shrinking the outer diameter. The two diameters approach each other, and the eventual coincidence of true and nominal densities terminates the procedure. As the contraction rate approaches zero, this dependence decreases sharply. Packing fractions between 0.642 and 0.649 are consistent with Berryman's extrapolation.

Nolan and Kavanagh [30] proposed that the characteristics of random packing are determined by its interstices. They defined interstices to be a network of channels passing through the lattice, rather than isolated regions of space. It was stated that the lattice is transformed from random loose packing to random close packing as the mean interstices volume decreases from a maximum to minimum. They generated an algorithm to simulate any random packing between random loose packing to random close packing. The packing density was calculated by measuring every complete and fractional sphere positioned within a radius of 5-sphere diameter to the center of lattice. A contact was defined when there was an overlap between two spheres. The mean overlap was defined to be 0.002 of the sphere diameter. The packing density ranged from

0.509 to a maximum of 0.638. The random loose packing was 0.52. The mean coordination number varied from 4.4 to 5.9 as the structure changed from random loose packing to random close packing. The radial distribution function for random close packing has peaks at 1.0 and a split peak at 1.725 and 1.97.

Adams and Matheson [31] simulated random close packing of hard spheres. The idea behind the method was to place a new sphere at the tetrahedral site nearest to the center of packing, thereby producing a spherical model. The packing fraction was reported to be 0.628.

Very few of the published articles applied the optimization technique in the packing problem. Hermann et al. [32] used the generalized Bernal model for liquids to create the multi-component liquid and amorphous metallic alloys structure. They show that the optimization of computer simulated random close packing models is a promising way to propose models with enhanced packing fraction and to specify the compositions and radii distributions required. They also presented a series of multi-component systems with enhanced packing fraction and proposed them as candidates for new bulk metallic glasses. Optimization techniques are widely used in the logistics field because of their ability to pack multiple stuffs in the confine space with a short period of calculation.

George and Robinson [33] developed a wall building approach to container packing, which has been very widely applied and has formed the basis of many variants. It fills the container in layers across its width. The depth of each layer is determined by the size of the first box packed into the layer. The procedure starts from one end of the container and attempts to keep an even workface over the cross section of the container. The filling scheme chooses a box type and then completes as many columns as possible.

Thapatsuwan et al. [34] described the development and application of an artificial immune system (AIS), particle swarm optimization (PSO) and a genetic algorithm (GA) for solving multiple container packing problems (MCPP) using the Microsoft Visual Basic. It was found that each algorithm's parameters were statistically significant with a 95% confidence interval. The best configurations were then used in a sequential experiment that compared the performance of the AIS, PSO and GA algorithms for solving 21 heterogeneous MCPP.

These optimization techniques can also be adapted in the sphere packing problem to reduce processing time of the packing process.

2.2 Spheres Packing Algorithm

The catalyst layer's structure has been developed using the sphere packing process in order to understand the electrochemical reaction that happens in PEMFC. Spheres in this packing process represent the carbon atoms because carbon is the common material for the catalyst layer [1]. As the van der Waals radius of carbon is equal to 1.7 angstrom then the sphere radius was assigned to 1.7 angstrom and the base side of the cubic container can be calculated by the following equation [35].

$$D = 2 \times r \times \sqrt[3]{N} \tag{2.1}$$

where D is the base side (angstrom), r is the sphere radius (angstrom) and N is the number of spheres.

The packing algorithm can be described as follows:

Step 1   3 random numbers, for *x*, *y* and *z*, were generated to give the initial coordinate of carbon sphere and record this coordinate.

Step 2   Generate another 3 random numbers for the second coordinate of the carbon sphere.

Step 3   Test the coordinate from step (2) if the coordinate from step (2) is the same as the coordinate from step (1) then repeat step (1) again, otherwise record this coordinate.

Step 4   Repeat steps (2) and (3) until the number of desired spheres were placed in the cubic.

Step 5   Select a random number ($p_{current}$) within [0 , α] range where α is a parameter which controls the width of random number pool.

Step 6   Generate a random vector which has a magnitude of $p_{current} \times r$.

Step 7   Allow sphere number *i* to move along this vector.

Step 8   Test the current coordinate of this sphere to make sure that it does not overlap with other spheres. If the current coordinate of sphere number *i* overlaps with other spheres then repeat step (6).

Step 9   Repeat steps (6) to (8) until all spheres have been moved. Assign this configuration as a current configuration.

Step 10   Calculate the total potential energy of this configuration using the combination between the Lennard-Jones potential and the Morse potential which can be shown as the following formula.

$$L(r_{ij}) = 4\varepsilon[(\sigma / r_{ij})^{12} - (\sigma / r_{ij})^{6}]$$ (2.2)

Equation (5) shows the Lennard-Jones potential: $L(r_{ij})$ is the total Lennard-Jones potential

energy of the system (kJ per mol), ε is the Lennard-Jones potential for carbon-carbon

interaction which equals to 0.4396 kJ per mol, σ is the finite distance at which the inter-

particle potential of carbon-carbon is zero which equals to 3.851 angstrom [36] and r_{ij} is

the distance between two particles (angstrom).

$$M(r_{ij}) = \varepsilon_m [e^{-2\alpha(r_{ij}-r_0)} - 2e^{-\alpha(r_{ij}-r_0)}] \tag{2.3}$$

Equation (6) shows the Morse potential [37] where $M(r_{ij})$ is the total Morse potential

energy of the system (kJ per mol), ε_m is the Morse potential parameter which equals to

478.9 kJ mol^{-1}Å^2, α is a parameter that controls the width of the potential and it is equal

to 2.1867 Å^{-1} , r_0 is the equilibrium bond distance which equals to 1.418 Å [36] and r_{ij} is

the distance between a pair carbon molecules. The total potential energy of the system

can be written as $U(r_{ij}) = L(r_{ij}) + M(r_{ij})$.

The objective function of this process is to minimize the total potential energy.

Each packing configuration will be at the steady state when the total potential energy of

that configuration reaches the global minimum. Step 1 to step 10 in this algorithm are

similar to the basic random search technique (BRST) [38] and the flow chart of this

BRST is shown in Figure 2.1.
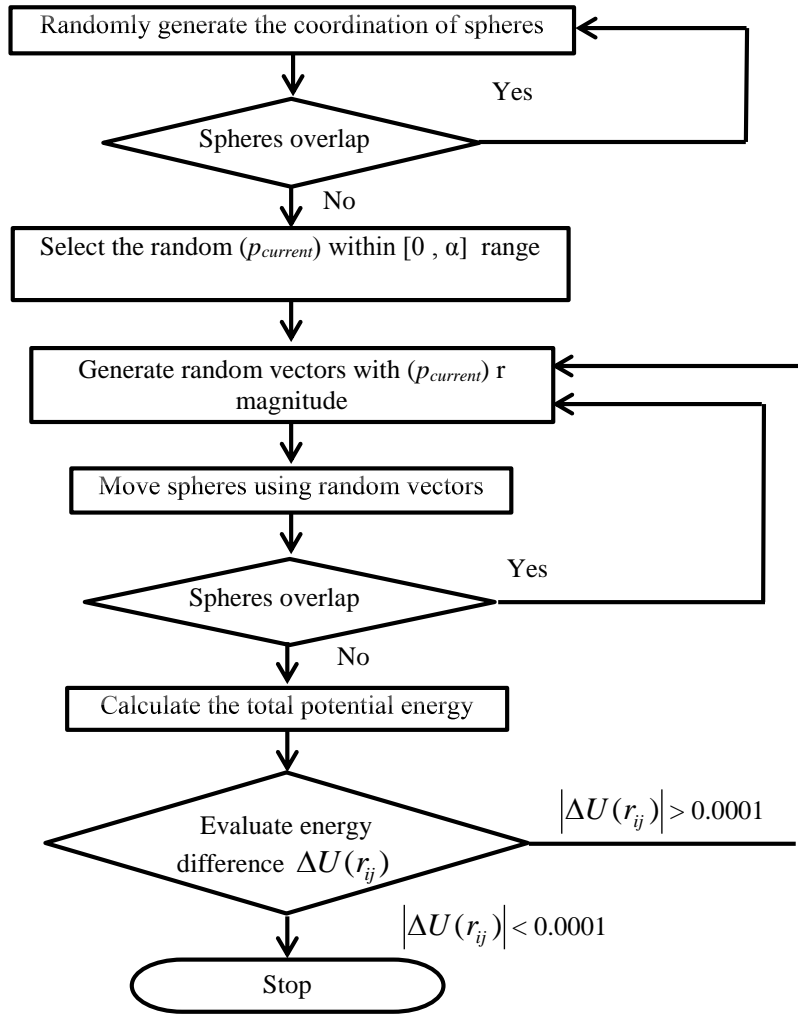
Figure 2.1. Flow chart of the BRST algorithm.

Even though the BRST algorithm gives a very good chance to reach the global minimum for the objective function but the drawback of the BRST algorithm is it takes too much time before reaching that global minimum solution [38]. To decrease the processing time of the packing process, an optimization technique called the adaptive random search technique (ARSET) [38] is applied which allows us to vary the magnitude of random vectors based on the difference of total potential energy. Detail of this technique can be found in step 11 through step 19.

Step 11 Select a random number (q) within $[0\,,\,\alpha]$ range. This random number, q, is be

used to increase or decrease the magnitude of initial random vector.

Step 12 Generate a random vector which has a magnitude of $p_{current} = (p_{current} + q) \times r$.

Step 13 Repeat steps (7) to (9) and assign this configuration as a new configuration.

Step 14 Calculate the total potential energy of this new configuration and find the

difference of the total potential energy between new and current configuration

which is described as the following equation.

$$\Delta U(r_{ij}) = U_{new}(r_{ij}) - U_{current}(r_{ij}) \tag{2.4}$$

where $U_{new}(r_{ij})$ is equal to a total potential energy from step (14) and $U_{current}(r_{ij})$ is equal

to a total potential energy from step (10).

Step 15   If $\Delta U(r_{ij})$ is less than zero then change the value of α using this following

equation.

$$\alpha_{new} = \alpha_{current} * (U_{current} / U_{new}) \tag{2.5}$$

Step 16 Repeat steps (11) to (15) until the absolute potential energy difference is less

than 0.0001 and stop the program.

Step 17 From step (14) if $\Delta U(r_{ij})$ is greater than zero then generate random vectors

which have a magnitude of $p_{current} = (p_{current} - q) \times r$ and repeat steps (13) to

(15) again.

Step 18 If $\Delta U(r_{ij})$ is still greater than zero then change the value of α using equation

(5).

Step 19   Repeat upper steps until the potential energy difference is less than 0.0001 and

stop the program.

The difference between the BRST and the ARSET is that the BRST has not

considered the random vectors variation. The BRST does fix the magnitude of the

random vector at ($p \times r$) and repeats the procedure until the potential energy difference is

less than 0.0001 then stop. But for the ARSET algorithm, it changes the magnitude of

random vectors based on the current solution and new solution. Furthermore the benefit

of this ARSET algorithm is simplicity, it doesn't require any differentiation and it is easy

to understand which makes this ARSET adaptable to scientific and engineering problems.

Flow chart of the ARSET algorithm is shown in Figure 2.2.
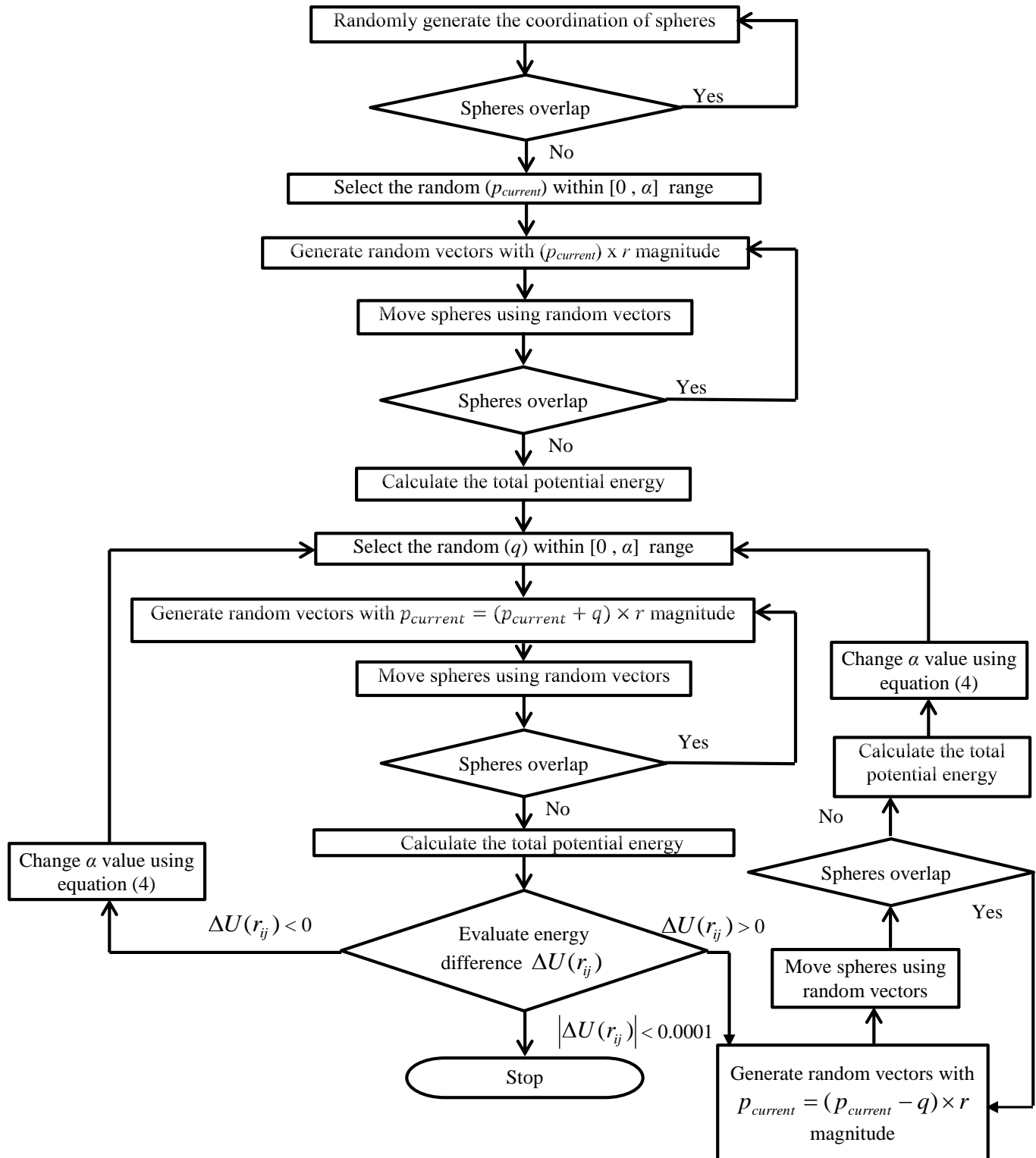
Figure 2.2. Flow chart of the ARSET algorithm.

This self-developed program is written in Mathematica code and the specifications of the computer hardware that used to run this code is described in Table 2.1.

Table 2.1

Computer hardware specifications

Component	Specification
CPU	Intel Core i5 450M
RAM	PC3-8500F: 8 GB
Hard Drive	SATA 2 7200 RPM with 16 MB Cache
Operation system	Windows 7 64 bits

The solid fraction of each run was calculated, after the end of each packing process, by dividing the solid volume by the total volume. The initial value of α is equal to 0.5 and we investigate the effect of this α value which is described in the last section of this chapter.

2.3 Results and Discussion

2.3.1 Algorithm verification

Because the results from the BRST algorithm always reaches the global minimum [38] then the total potential energy results from the ARSET algorithm are compared with the results from the BRST algorithm to ensure that results from this adaptive algorithm also reached the global minimum. One hundred different initial configurations each for the systems of 1000 spheres, 1800 spheres, 5000 spheres, 10000 spheres and 30000 spheres are generated, each of them has a different initial total potential energy, and

allowed to complete the packing process using the BRST or the ARSET algorithm. The average total potential energy for each number of spheres from the BRST algorithm and the ARSET algorithm are calculated and the results of these tests are shown in Table 2.2.

Table 2.2

Average final total potential energy from the BRST and the ARSET algorithms

| | Average total potential energy | | |
Number of spheres	BRST	ARSET (σ = standard deviation)	% difference
1,000	0.0914	0.0914 (σ = 0.00015)	0%
1,800	0.0917	0.0919 (σ = 0.00014)	+0.2181%
5,000	0.0923	0.0927 (σ = 0.00018)	+0.4333%
10,000	0.0974	0.0992 (σ = 0.00028)	+1.8480%
30,000	0.0962	0.0999 (σ = 0.00037)	+3.8461%

As shown in Table 2.2, after finished the packing process using the BRST algorithm, the total potential energy for each number of spheres converged to a certain number which is a global minimum state for the total potential energy. Differences between the average final total potential energy from the BRST and the ARSET algorithms are less than 0.5% when the number of spheres is less than 5,000 but the percentage differences are equal to 1.85% and 3.86% for the system of 10,000 and 30,000 spheres, respectively. From these results, the performance of the ARSET algorithm tends to decrease as the number of spheres increase. Complexity of the search space will increase as number of spheres increases and this complexity will affect the search ability of this ARSET algorithm. Even though the ARSET algorithm still shows some errors when the number of spheres is greater than 5000, these errors are still small, less than

4%, which indicated that the ARSET algorithm is acceptable. The total potential

energies from the ARSET are about 4% higher than the total potential energy from the

BRST which means that the packing configurations from the BRST are more stable than

the configurations from the ARSET. To interpret the effect of these configurations, the

solid fraction for each number of spheres must be incorporated and the discussion about

the solid fraction can be found in the next section.

The developed ARSET algorithm was proved to give the global minimum for the

total potential energy. The next step is to verify the results from this ARSET algorithm

with previous results published by [29] and [30]. We ran this program for 100 times for

1,000 spheres and 1,800 spheres. The average solid fractions were computed and

compared with the previous works. For 1,000 spheres, our solid fraction is equal to

0.621, compared with 0.645 from [29] which is approximately 3.72% lower than the

reference value. But for 1,800 spheres our solid fraction is equal to 0.624 compared with

0.635 from [30] which is 1.73% different from the reference value. Detail of this

comparison is shown in Table 2.3.

Table 2.3

The average solid fraction

Number of spheres	Reference calculated solid fraction	Current calculated solid fraction	% difference
1,000	0.645 [29]	0.621	-3.720%
1,800	0.635 [30]	0.624	+1.732%

From the results shown in Table 2.3, the solid fraction obtained from this ARSET algorithm has good agreement with the solid fractions obtained from previous works which means that this developed ARSET algorithm yields the acceptable results.

2.3.2 Benefit of the developed ARSET algorithm

This developed ARSET algorithm has been used the difference between the current potential energy and the potential energy from the next step to change the magnitude of the random vectors. This means that the ARSET algorithm expands or narrows the search space. If this ARSET yielded the better solution then it expands the search space. Otherwise, it narrows down the search space if a better solution has been found after the expansion.

From this concept the developed ARSET algorithm should reduce the chance of obtaining the local minimum solution and accelerate to the global minimum solution which can decrease the processing time of the packing process.

To prove that the developed ARSET algorithm can reduce the processing time, we ran this program for five different numbers of spheres using the BRST and the ARSET algorithms. The simulation for each number of spheres was run for 100 times. Actual processing time and solid fraction value were recorded after the end of each run. These numbers were used to calculate the average actual processing time and the average solid fraction value.

From the results shown in Table 2.4, the developed ARSET algorithm reduces the actual processing time by 5.58% to 34% depend on the number of spheres. When the number of spheres increases, the developed ARST algorithm will significantly reduce the amount of actual processing time. But for the case of 30,000 spheres, the performance of this ARSET algorithm is less than that of 10,000 spheres case. This phenomenon is the result of the system complexity. For 30,000 spheres case, this ARSET algorithm moved 30,000 spheres and calculated the total potential energy for each move this might yield a number of local minimums which the ARSET algorithm has to get rid of in order to obtain the global minimum result. In order to get past this local minimum, the ARSET algorithm has to move back and forth, expands or narrows the search space which has consumed the processing time and lowers the performance of the packing process.

Table 2.4

Actual processing time comparison between the BRST and the ARSET algorithms

	Actual processing time (second)		
Number of spheres	BRST	ARSET	% difference
1,000	0.39	0.37	-5.58%
1,800	0.58	0.50	-13.79%
5,000	16.81	13.05	-22.36%
10,000	98.34	64.32	-34.59%
30,000	1308.73	936.81	-28.42%

In general, the ARSET algorithm has already been proved to be more effective than the BRST algorithm and the next step is to compare the solid fraction of these two algorithms.

The value of solid fraction from these five different numbers of sphere using the BRST and the ARSET algorithms are very similar. Results in Table 2.5 show that for 1,000 and 1,800 spheres cases solid fractions from these two algorithms are the same, but for 5000, 10000 and 30,000 spheres the values of solid fraction obtained from the BRST and the ARSET are slightly different.

Table 2.5

Solid fraction comparison between the BRST and the ARSET algorithms

	Solid Fraction		
Number of sphere	BRST	ARSET	% difference
1,000	0.621	0.621	0%
1,800	0.624	0.624	0%
5,000	0.625	0.617	1.280%
10,000	0.628	0.611	2.707%
30,000	0.629	0.610	3.021%

As seen in Table 2.2, the total potential energy from the BRST and the ARSET algorithms for 5000, 10000 and 30,000 spheres cases are different which means that the packing configuration from the BRST and the ARSET algorithms for these three cases are also different too. The total potential energy values from the ARSET algorithm are higher than the total potential energy from the BRST algorithm which means that the packing configurations from the BRST algorithm are more stable than the configurations from the ARSET algorithm. Furthermore, the results from Table 2.5 can be incorporated with the results from Table 2.2 which concludes that the packing configurations from the ARSET are less dense. These less dense packing configurations allows more protons and

oxygen molecules transport but they also lowers the electron conductivity. The effect of these phenomena need to be investigated in the future study.

2.3.3 Magnitude of the random number and its effect

In the ARSET algorithm, spheres are allowed to move along the random vector while the magnitudes of these random numbers are limited by the value of α. Then in this section, the effect of α is investigated by initially selects three α values and runs the ARSET algorithm for three different numbers of spheres which are 5000, 10000 and 30,000 spheres. The initial α values that were selected for this test are 0.3, 0.5 and 0.7. Each case has been processed for 100 times and the average actual processing time of each case is calculated which are shown in Figure 2.3 to Figure 2.5.

From Figure 2.3 to Figure 2.5, the initial α values show some effects in the actual processing time.
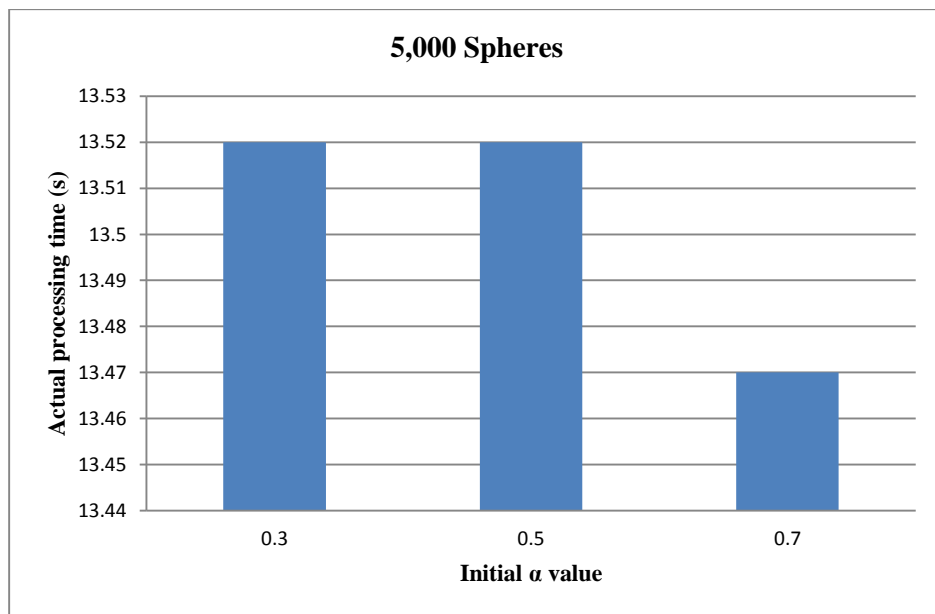
Figure 2.3. The average actual processing time for 5,000 spheres.

From Figure 2.3, the initial α value equal to 0.7 gives the processing time equal to 13.47 seconds compared to 13.52 seconds of the initial α value equal to 0.3 and 0.5 then for 5,000 spheres case the initial α value of 0.7 is considered to be the best.

In Figure 2.4 the initial α value equals to 0.7 is still better than the initial α value of 0.3 and 0.5 because it yields the lowest processing time equal to 75.55 seconds compared to 84.13 seconds and 80.47 seconds of the initial α values equal to 0.3 and 0.5, respectively.
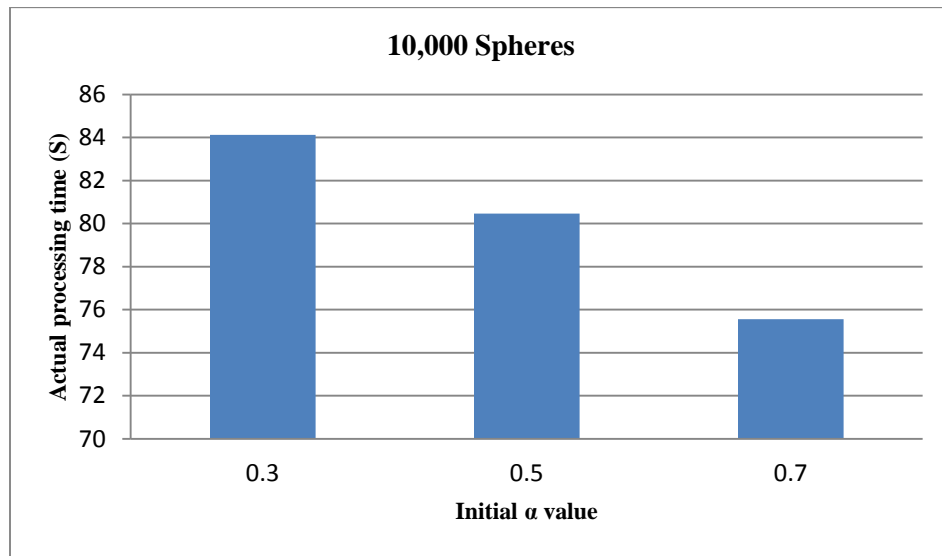
Figure 2.4. The average actual processing time for 10,000 spheres.

But for 30,000 spheres the initial α value equals to 0.7 yields the longest processing time of 1,097.08 seconds compared with 990.38 seconds of initial α value equals to 0.3 and 1,012.75 seconds of initial α value equal to 0.5.
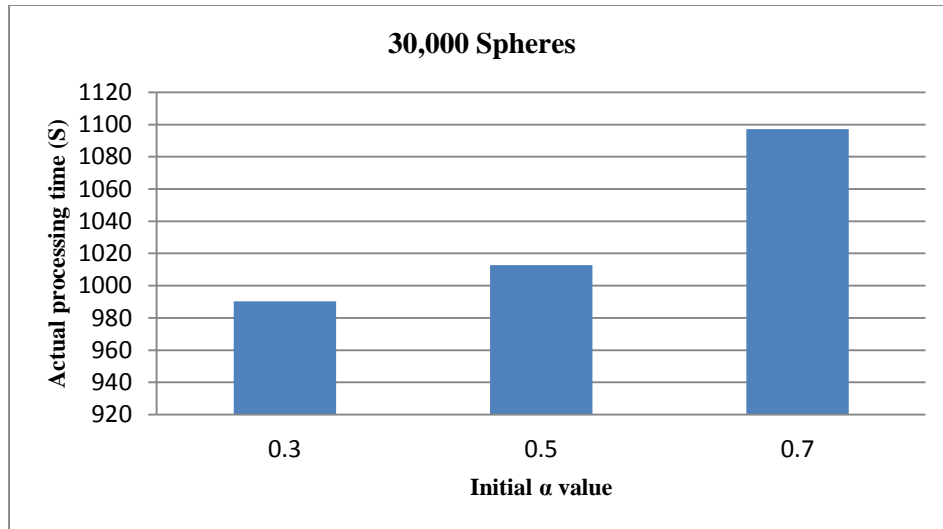
Figure 2.5. The average actual processing time for 30,000 spheres.

From the nature of the ARSET algorithm, the magnitude of random vectors is changed to the optimized value as the packing process is continuously running. The magnitude of random vectors is increased or decreased until they found the global minimum and if the difference between initial α value and the desired α value is large then the actual processing time is also large. As the initial α value equals 0.7 yields the longest processing time for 30,000 spheres cases and the initial α value equals 0.3 yields the longest processing time for 10,000 spheres case then we suggest using the moderate initial α value of 0.5 to be the universal initial α value because it gives moderate processing times for 5,000 and 30,000 spheres cases and the shortest processing time for 10,000 spheres.

The ARSET algorithm has been proved to be the effective algorithm for the sphere packing process. It not only reduces the actual processing time but also gives the good results compared with another algorithm. Figure 2.6 and Figure 2.7 show the

simulation results of 5,000 and 10,000 spheres using the developed ARSET algorithm

with the initial α equal to 0.5.
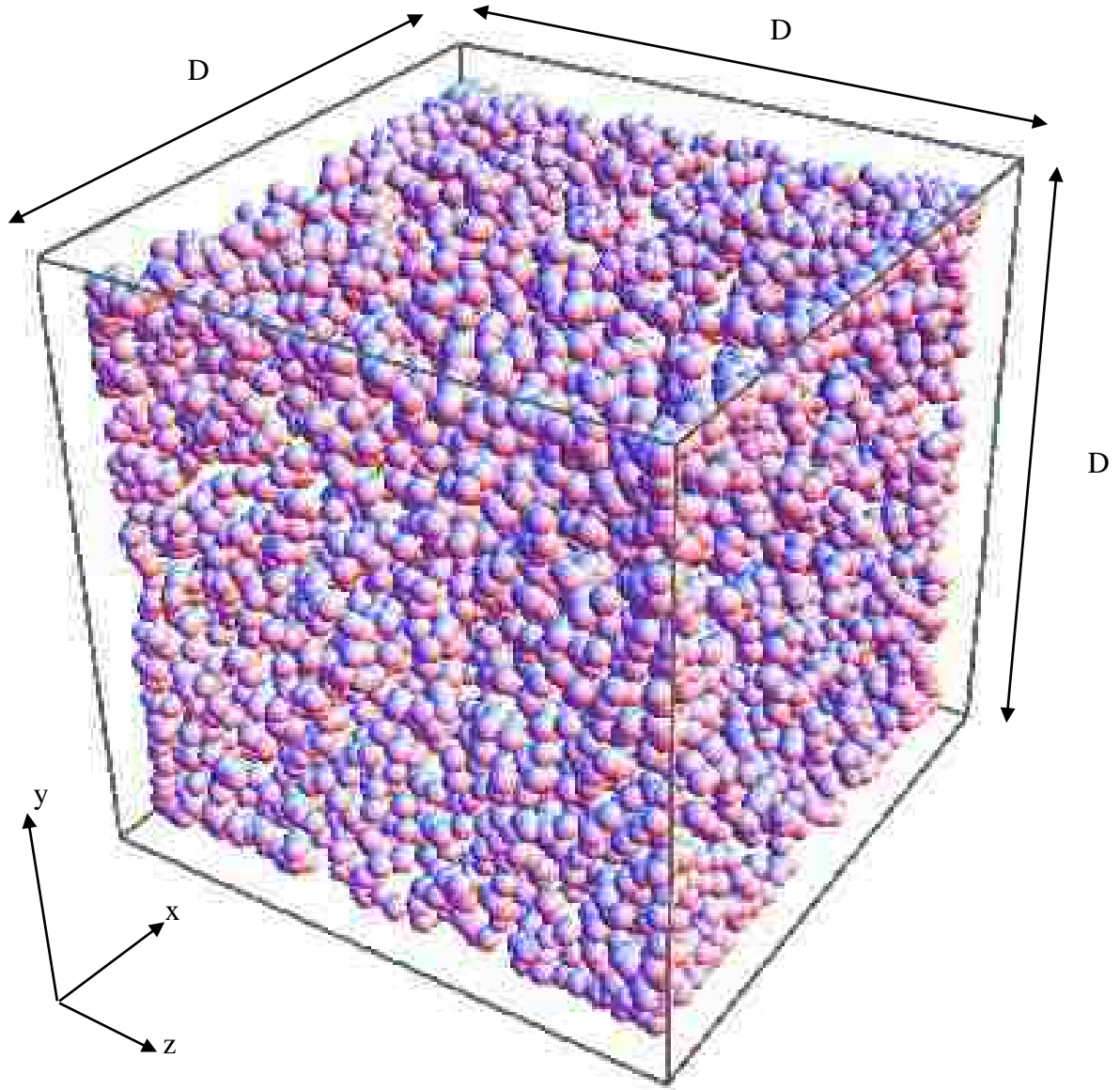
Figure 2.6. Sphere packing simulation result for 5,000 spheres with the initial $\alpha = 0.5$.
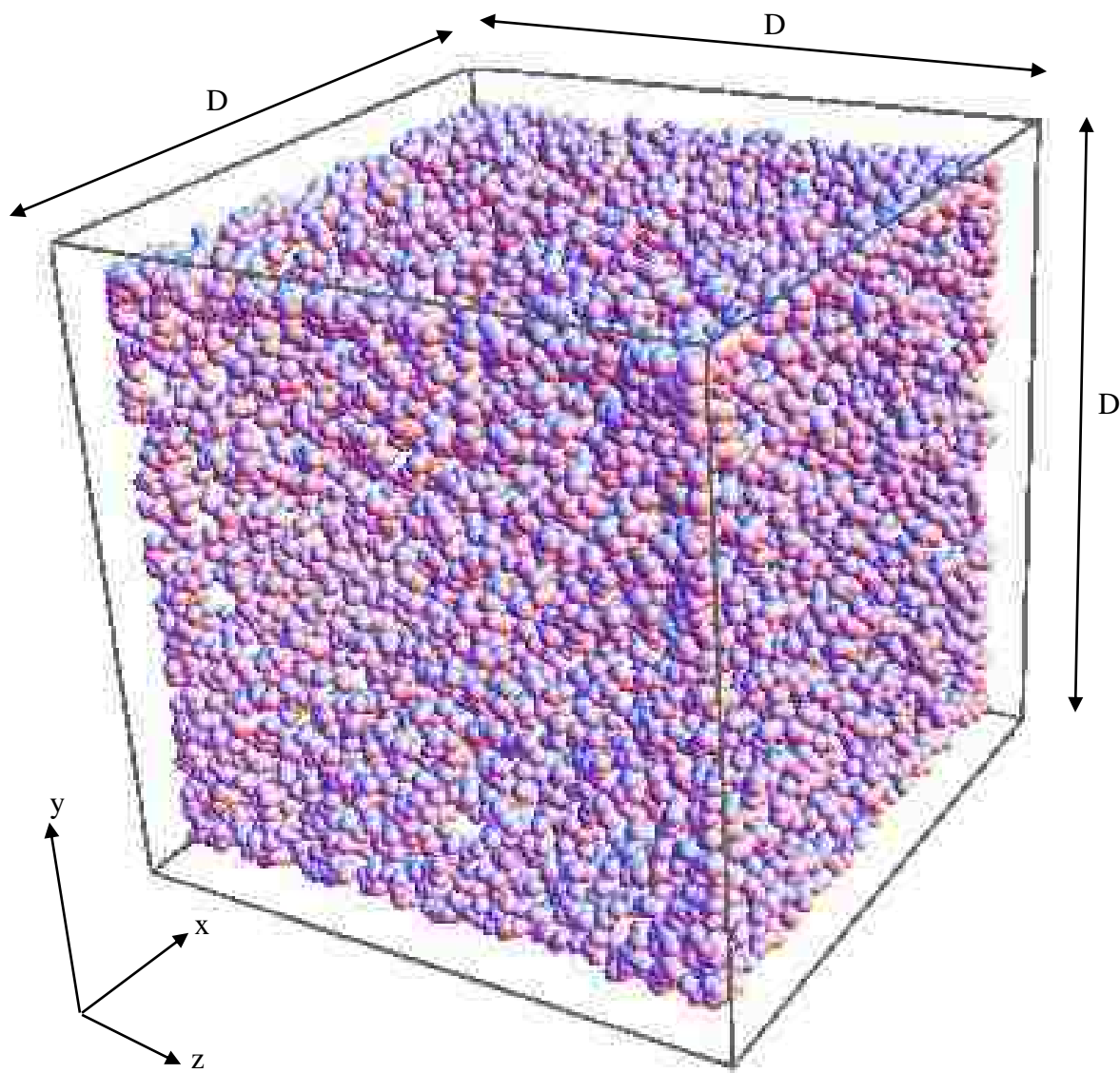
Figure 2.7. Sphere packing simulation result for 10,000 spheres with the initial α = 0.5.

Each sphere represents a carbon atom which is packed to form the atomistic

structure of the catalyst layer. From Table 2.5, the solid fractions of these two cases are

equal to 0.617 and 0.611 respectively which mean that these catalyst layers have

approximately 38% void space. This void space will allow proton and oxygen molecules

to diffuse through and these molecules which will later be interacted which each other

and form water molecules. These water molecules must be expelled from the catalyst layer in order to maintain the best performance of fuel cell.

The movement of protons and, oxygen and water molecules is limited by the void space. If the catalyst layers have large void space then protons, oxygen and water can easily diffuse through the catalyst layers but the electron conduction through carbon molecules is lower than the case of small void space. These simulated catalyst layers will be used to model the diffusion of proton, oxygen and water at the cathode side of PEMFC and the effect of the void space will be investigated in the later chapters.

2.4 Conclusions

An optimization technique and computer code called the adaptive random search technique (ARSET) has been successfully developed and employed in the sphere packing algorithm. This ARSET algorithm can vary the magnitude of random vectors based on the total potential energy difference between current and new configuration. This ARSET algorithm has been proved that it can give the global minimum solution for the total potential energy. When apply this algorithm to 1,000 and 1,800 spheres, it gives a good agreement in solid fraction values compared with the results from the previous works.

This developed ARSET algorithm significantly reduces the actual processing time of the packing process compared with the basic random search technique (BRST) algorithm. The actual processing times that can be reduced using this algorithm are 5.58% for the system of 1,000 spheres, 15% for the system of 1,800 spheres, 22% for the

system of 5,000 spheres, 34% for the system of 10,000 spheres and 28.42% for the system of 30,000 spheres. The solid fractions from the BRST and the ARSET algorithms are very similar with the maximum percentage difference at 2.73%. The effect of initial sampling range (α) has also been investigated and the appropriate α value is equal to 0.5 because it shows a good performance with any number of spheres.

CHAPTER 3

DIFFUSION AND CHEMICAL REACTION IN PEMFCS CATHODE

CATALYST LAYER

3.1 Introduction

As PEMFCs are energy conversion devices, they can convert the chemical energy which is stored in their fuel, which are hydrogen and oxygen, into electrical energy and water. This excess product water must be repelled out of cathode catalyst layer otherwise it can block the movement of protons and oxygen molecules which can dramatically reduce the performance of fuel cells. To improve the performance of PEMFCs, appropriate water management strategies should be introduced and the best way to develop these water management strategies is to investigate how water is created and moved out of the cathode catalyst layer which means this study is focused at the atomic level. Scholars have proposed many simulation models using the Monte Carlo (MC) technique to study the transport phenomena in fuel cell.

Seidenberger et al. [39] introduced the MC model which requires low computational resource but it still can simulate the liquid water distribution within the GDL on the micro scale. Their result shows a clear influence of the porous polytetrafluoroethylene (PTFE) coverage upon the amount of water residing within the GDL structure. When decreasing the PTFE coverage area more and more water clusters are formed until they reach a critical value which is very important for fuel cell operation.

Seidenberger et al. [40] improved their former MC model and shifted the focus to the liquid-solid phase boundaries and the phase transitions. Their simulation results show that the GDL region is especially prone to the accumulation of liquid water.

Modak and Lusk [41] have developed a kinetic Monte Carlo (KMC) model which simulates the open circuit voltage in a doped electrolyte. Their work was focused on electrical–physical processes but did not consider any chemical reactions. A pressure differential was applied over an uncharged and open-circuited electrolyte allowed to come to equilibrium. The voltage was computed as a function of time and found to reach the values predicted by equilibrium thermodynamics over a range of pressure differentials. Results from the Monte Carlo simulation were compared with the predictions from an analytical model and were found to be in a very good agreement.

Wanga et al. [42] studied a hydrogen-powered solid oxide fuel cell (SOFC) using a kinetic Monte Carlo model. Its electrolyte, cathode, and anode are 9 mol% yttria stabilized zirconia (YSZ), ultrathin metal Pt, and ultrathin metal Ni, respectively. Chemical reactions at the cathode and anode side of the fuel cell were simulated. The ionic current density (J) is used to perform a sensitivity analysis for the kinetic parameters by varying the operating condition under the different materials. Result from their simulation shows that the amount of input oxygen which is the main factor for the fuel cell performance is followed by the oxygen ion transfer within YSZ. Physical parameters such as the applied bias voltage, operating temperature, thickness of the YSZ, and the relative permittivity of the YSZ are found to significantly affect the calculated ionic current density of the SOFC.

Lau et al. [43] developed a KMC model to simulate the cathode of an YSZ fuel cell using a nonsymmetrical cell scheme. In their model, the oxidation reduction reaction that occurs at the SOFC cathode was simulated at the atomic level. The ionic current density (J) is used to evaluate the limitations of the cathode/YSZ performance. Material properties and different operating conditions are also evaluated. According to the results of their simulation (1) temperature, (2) dopant fraction of Y_2O_3, and (3) the relative permittivity of YSZ are found to be the critical parameters for the performance of fuel cell.

Ge et al. [44] introduced a two-dimensional Markov Chain Monte Carlo model for the anode/electrolyte interface. The density of oxygen vacancies, which is directly adjacent to the lanthanum strontium vanadate (LSV) / YSZ interface, is one order of magnitude higher than the bulk value of YSZ. The double layer undergoes pronounced relaxations when the interfaces are under anodic biases ranging from 0 to 150 mV. The results indicate that 70–80% of the oxygen vacancies are immobilized in the Helmholtz–Perrin layer. The rationale presented in this work has wide applications on elucidating anodic reaction mechanisms and potential distributions across anode/electrolyte interfaces.

Zhange et al. [45] developed a two phase lattice model of electrode catalyst layer in PEMFC which incorporated a catalyst-mixed ionomer and pores using the Monte Carlo method. Their model proves to be more accurate compared to another two phase lattice model which has the catalyst layer composition consisting of a pore phase and a mixed electronic and ionic conductor phase. The peak of the reaction rate moves from membrane side to the GDL side with the increase of cell current, as a result of rate-

limiting factor shifting from proton conduction to oxygen transport. Nonuniform

ionomer distribution across catalyst layer, with higher ionomer content at the membrane

side and higher porosity at GDL side, is superior to uniform ionomer distribution when

working at high cell current.

Suzuki et al. [46] developed a three-dimensional modeling for the cathode catalyst

layer of a PEMFC which is made from 20 wt% Pt/C. The pore tortuosity of the cathode

catalyst layer was calculated using the systematic development of a numerical simulation.

The simulated results of current density-potential curves indicated the existence of an

optimum ionomer content (33%) for a PEMFC catalyst layer. The effect of the

electrolyte content on the oxygen diffusion coefficient and proton conductivity of the

cathode catalyst layer (CCL) was also investigated. The proton conductivity increased

with an increase in the ionomer content. In contrast, the oxygen diffusion gradually

decreased as the ionomer content increased. The relationship among a network of

catalyst grains for electronic conduction, a network of ionic conduction and a network of

channels for gas diffusion were investigated to formulate a correlation between the

ionomer percentage and a polarization characteristics. At an optimal ionomer content,

both carbon grains and the ionomer were found to be perfectly percolated.

The cathode catalyst layer, which is the location where the electrochemical

reaction happens, is one of the most important regions to study the transport phenomena

in PEMFCs. The structure of the cathode catalyst layer which is a porous media [1] is

very important for the transport phenomena of proton, oxygen and product water. The

movement of protons and oxygen and water molecules is limited by void space. Protons,

oxygen and water have to diffuse through the catalyst layers using this void space to be

41

their path for movement. The complexity of the cathode catalyst layer (CCL) is an important variable for the diffusion of these three species. If the structure of the CCL is very complex then protons, oxygen molecules and water molecules cannot be easily diffused through it. In this study, the Monte Carlo simulation is used to model the transport phenomena in the cathode catalyst layer. To understand how water is created in the catalyst layer the electrochemical reaction between protons and oxygen has to be simultaneously considered and included in this numerical simulation study.

3.2 Numerical Simulation Algorithm

The algorithm has been separated into two parts. The first part is the cathode catalyst layer formation using the spheres packing algorithm and the second part is the movement of proton, oxygen and water, which water is a product of the chemical reaction between proton and oxygen, through this developed cathode catalyst layer.

The basic material of the cathode catalyst layer is carbon with platinum (Pt) particle coated on its surface [1]. But in Chapter 2 only the carbon molecule is considered in the sphere packing algorithm. So in this chapter an assumption is made that those carbon molecules already have the Pt particles uniformly dispersed on their surfaces.

The sphere packing algorithm described in Chapter 2 has been modified by changing the shape of the container from cubic shape to rectangular shape because the normal shape of the cathode catalyst layer is rectangular not cubic. In the previous chapter the shape of the container is cubic which has a base side equal to D which can be calculated from equation (3.1):

$$D = 2 \times r \times \sqrt[3]{N}$$

where D is the base side (angstrom), r is the sphere radius (angstrom) and N is the number of spheres. But the new container's shape, which is rectangular, has a length of 2D, thickness of D/2 and the width of D, so these two containers still have the same volume which is D^3.

Z = 0   Z = D/2
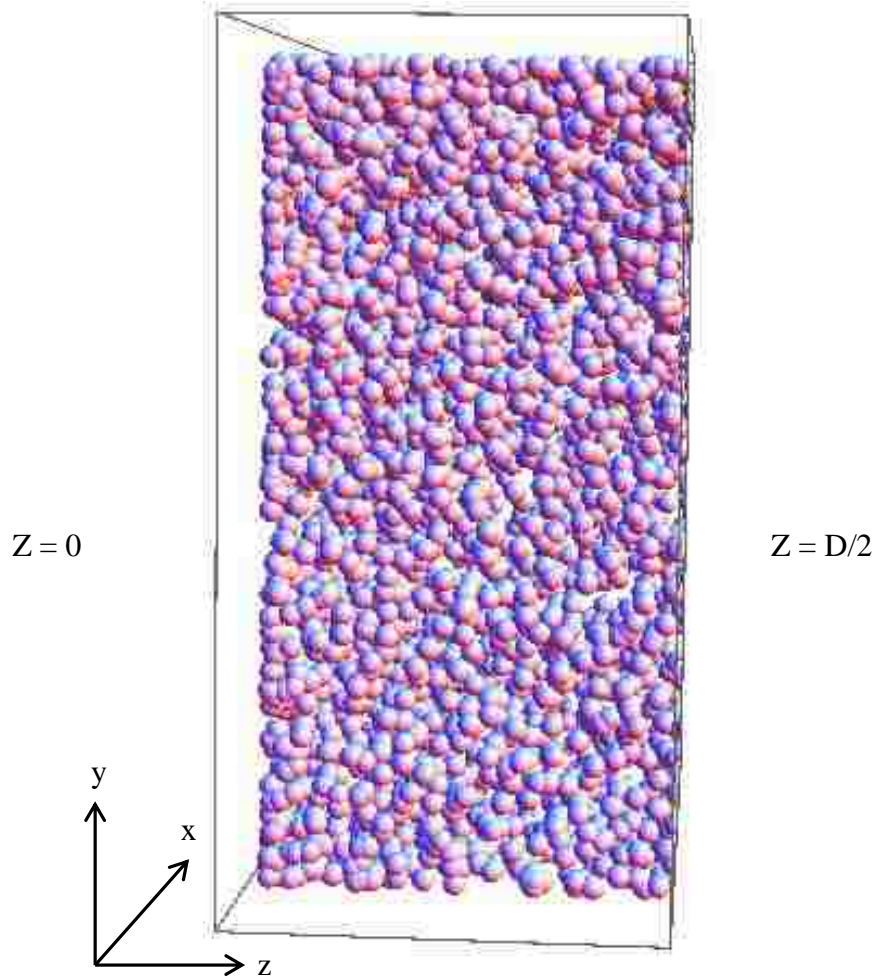
Figure 3.1. Packing result of 10,000 spheres in the rectangular container.

Figure 3.1 is the result of the spheres packing algorithm which represents the atomistic structure of the cathode catalyst layer, each sphere in the container is the carbon

molecule with the Pt particles uniformly dispersed on its surface. The solid fraction of this packing is equal to 0.611 or the void space of this packing is approximately 39%. Proton and oxygen will use this void space to diffuse into the cathode catalyst layer and interact with each other to form water molecule.

The thickness of the cathode catalyst layer is usually in the range of 10 μm [1] and from the packing algorithm the thickness (D/2) of the container can be calculated by equation (3.1). As the van der Waals radius of carbon is equal to 1.7 angstrom then the sphere radius was assigned to be 1.7 angstrom. If the cathode catalyst layer with the thickness of 10 μm is created and used then more than 25 billion carbon molecules need to be packed in the rectangular container and this will require the enormous computational time. Because the packing algorithm requires the clock time in the numerical simulation to be at least 1 minute to pack 10,000 carbon molecules and at least 15 minutes to pack 30,000 carbon molecules, the processing time will exponentially increase when the number of spheres increases which results in packing complexity. To deal with the packing processing time, the cathode catalyst layer which made of 10,000 carbon molecules is simulated or on the other hand the thickness of this simulated cathode catalyst layer is approximately 36 angstrom. From Figure 3.1, the thickness of this simulated catalyst layer is represented in the Z-direction while the length is represented in the Y- direction and the width in the X-direction.

The electrochemical reaction that occurs in the cathode catalyst layer can be represented in the following equation.

$$4H^+ + 4e^- + O_2 \rightarrow 2H_2O \qquad\qquad (3.2)$$

This chemical reaction is the combination of 4 species which are proton (H^+), electrons (e^-), oxygen (O_2) and water (H_2O). As proton cannot diffuse through the cathode catalyst layer by itself, it needs water as a media. Proton tends to interact with water to form a hydronium (H_3O^+) and this hydronium will diffuse through the cathode catalyst layer and interact with oxygen and form water molecules. This electrochemical reaction is investigated at the very beginning which includes the movement of hydroniums and oxygen into the cathode catalyst layer and the electrochemical reaction between hydroniums and oxygen. In this simulation, four assumptions have been made which are: (1) the electrochemical reaction among hydroniums, electrons and oxygen molecules is assumed to be isothermal; (2) the movement and the electrochemical reaction of electron are neglected based on the assumption that electron is one of the smallest particles which means it can easily conduct through the cathode catalyst layer and it should represent itself when hydroniums and oxygen tend to interact with each other; (3) the hydrogen bonding effect inside of the water molecules is not considered; (4) Brownian motion is not considered because each molecular movement is controlled by a random vector, which based on the Monte Carlo technique, and it replicates the Brownian motion.

The developed algorithm which controls the movement of hydroniums, oxygen and the product water is described as follows:

Step 1   Randomly generate the initial location of hydroniums and oxygen molecules, the initial location of hydroniums will have the coordinate of (x , y , 0) and oxygen molecules will have the initial coordinate of (x , y , D/2) where x and y are random numbers.

Step 2   Check if the location of hydroniums, oxygen molecules and carbon molecules, from the spheres packing algorithm, overlap with each other or not. If there is no overlap then go to step (3) otherwise go back to step (1).

Step 3   Generate a random vector which has a magnitude of 0.5 x r_o, where r_o is the van der Waals radius of oxygen which equals to 1.5 angstrom [47].

The reason of why the magnitude of the random vector for oxygen molecule is equal to 50 percent of the molecular radius is because oxygen molecule size is close to carbon molecule size, 1.7 angstrom, and this moving algorithm needs to make sure that these oxygen molecules continuously move through the cathode catalyst layer and they are not jumping through the void space. If the magnitude of the random vector is too long then there is a chance that the molecule will not move on its path and, instead, will jump from the initial location to the final location. The latter is big enough for it to fit in, even though the size of that moving channel is smaller than the molecular size. If the magnitude of the random vector is small enough then this molecule has to check the possibility of its every moving step so that every moving channel must be possible for this molecule to move through in order to complete the moving step in the developed algorithm.

Step 4   Allow oxygen number i to move along this vector.

Step 5   Test if the current coordinate of this oxygen overlaps with other molecules or not. If the current coordinate of oxygen number i overlaps with other molecules then go to back to step (3) otherwise go to step (6).

Step 6   Repeat steps (3-5) until all oxygen molecules are moved and save this

configuration as the new configuration.

Step 7   Calculate the total potential energy of this current configuration using the

Lennard-Jones potential which is shown by the following equation.

$$L(r_{ij}) = 4\varepsilon[(\sigma/r_{ij})^{12} - (\sigma/r_{ij})^{6}] \qquad (3.3)$$

Equation (3.3) shows the Lennard-Jones potential where $L(r_{ij})$ is the total Lennard-Jones

potential energy of the system (kJ per mol), ε is the Lennard-Jones potential (kJ per

mol), σ is the finite distance at which the inter-particle potential energy of carbon-

carbon is equal to zero and r_{ij} is the distance between 2 particles (angstrom).

Step 8   Generate a random vector which has a magnitude of 0.5 x r_h, where r_h is the

atomic radius of hydronium which equals to 1.43 angstrom [48]. The Lennard-

Jones potential parameter of hydronium is taken from Gertner and Hynes [49]

and the full description of the Lennard-Jones potential used in this simulation can

be seen in Appendix B. In order to determine the Lennard-Jones parameter of

each molecular pair, the Lorentz/Berthelot mixing rules is utilized. The

Lorentz/Berthelot mixing rules is an arithmetic equation which can estimate the

intermolecular potential parameters for a mixed pair of molecules by combining

the analogous potential parameters for the two pairs of identical molecules (ii

and jj). The Lennard-Jones mixed pair parameter can be calculated by the

Lorentz/Berthelot mixing rules using the following equations:

$$\sigma_{ij} = \frac{1}{2}(\sigma_{ii} + \sigma_{jj}) \qquad (3.4)$$

47

where σ_{ij} is the finite distance (angstrom) at which the inter-particle potential of a mixed pair molecule is zero.

σ_{ii} and σ_{jj} is the finite distance (angstrom) at which the inter-particle potential of identical molecule is zero.

$$\varepsilon_{ij} = \sqrt{\varepsilon_{ii}\varepsilon_{jj}} \qquad (4.2)$$

where ε_{ij} is the Lennard-Jones potential for mixed pair interaction (kJ per mol).

ε_{ii} and ε_{jj} is the Lennard-Jones potential for identical molecules (kJ per mol). The reason that the magnitude of the random vector is set to 50 percent of the molecular radius for hydronium is based on the similar reason and assumption for oxygen molecule which is described in step 3.

Step 9   Allow hydronium number i to move along this vector.

Step 10 Test if the current coordinate of this hydronium overlaps with other molecules or not. If the current coordinate of hydronium number i overlaps with other molecules then go to back to step (8) otherwise go to step (11).

Step 11 Repeat steps (8-10) until all hydroniums have been moved and save this configuration as the current configuration.

Step 12 Calculate the total potential energy of this current configuration using the Lennard-Jones potential.

Step 13 Calculate the total potential energy difference between step (12) and step (7) which is described as the following equation:

$$\Delta U(r_{ij}) = U_{new}(r_{ij}) - U_{current}(r_{ij}) \qquad (3.4)$$

where $U_{new}(r_{ij})$ is equal to a total potential energy of the new configuration and

$U_{current}(r_{ij})$ is equal to a total potential energy of the current configuration.

Step 14 If $\Delta U(r_{ij})$ is less than zero then accept the new configuration as current

configuration and go to step (15) otherwise go back to step (8).

Step 15 Check the oxygen molecules number i if there are four hydroniums located

within the length of 1 angstrom from the center of this oxygen molecule. If

there are four hydroniums located within this length then the electrochemical

reaction will happen because the hydrogen bond length in the water model is in

the range of 1 angstrom [50]. After this electrochemical reaction occurs, six

water molecules will replace those four hydroniums and oxygen molecule. The

coordinate of these newly-formed water molecules will be at the center of the

replaced hydroniums and oxygen. If there are no hydroniums within 1 angstrom

length then this algorithm will check oxygen molecules number $i+1$ for the

possibility of this electrochemical reaction.

Step 16 Repeat step (15) until all oxygen molecules are tested.

Step 17 Generate a random vector which has a magnitude of 0.5 x r_w, where r_w is the

van der Waals radius of water which equals to 1.41 angstrom [50].

The reason that the magnitude of the random vector is set to 50 percent of the molecular radius for water molecules is based on the similar reason and assumption for oxygen molecule which is described in step 3.

Step 18   Allow water number *i* to move along this vector.

Step 19   Test if the current coordinate of this water molecule overlaps with other molecules or not. If the current coordinate of water number *i* overlaps with other molecules then go back to step (17) otherwise go to step (18).

Step 20   Repeat steps (17-19) until all water molecules have been moved and save this configuration as the new configuration.

Step 21   Calculate the total potential energy of this new configuration using the Lennard-Jones potential.

Step 22   Calculate the total potential energy difference between step (21) and step (12).

Step 23   If $\Delta U(r_{ij})$ is less than zero then accept the new configuration as the current configuration and go to step (24) otherwise go back to step (17).

Step 24   Increase the number of iterations (*t*) by one and check the current value of the iteration if it is still less than the desired iteration then go back to step (1) otherwise stop. The flow chart of this algorithm is shown in Figure 3.2.

Initial or re-entry

Number of step greater than t — Yes → Stop

No

Randomly generate the coordination of hydroniums and oxygen molecules

Molecules overlap — Yes

No

Generate random vectors

Move hydroniums and oxygen molecules using random vectors

Molecules overlap — Yes

No

Calculate the total potential energy

Evaluate the possibility of the moving step — No → Reject this move

Yes

Electrochemical reaction — No → Check another oxygen molecule

Yes

6 water molecule will replace 4 hydroniums and 1 oxygen molecule

Generate random vectors

Move water molecules using random vectors

Molecules overlap — Yes

No

Calculate the total potential energy

Evaluate the possibility of the moving step — No → Reject this move

Yes

Figure 3.2. Flow chart of the developed algorithm for the pure catalyst layer.

51

In the real practice each molecular movement will affect the whole system, because of the intermolecular force, then every molecules should move together to simulate the actual behavior of the diffusion process. But this simulation algorithm, for each step, considers only the movement of a single molecule while another molecules are fixed which a limit of the Monte Carlo technique is. Unlike the Monte Carlo, molecular dynamic technique can be used to simulate the movement and the interaction of multiple molecules but it requires a powerful computational hardware an enormous processing time. To study the effect of the input hydronium and oxygen to the water distribution inside the cathode catalyst layer after the certain iteration, the input hydroniums and oxygen per iteration is varied as 3:2, 5:3 and 6:4 to determine which ratio yields the best result. Each successfully iteration can be roughly estimated as 4.38×10^{-13} second i.e. 0.438 picosecond and the simulation is allowed to run for 1000, 5000 and 20000 iterations to investigate the effect of time.

3.3 Results and Discussion

3.3.1 Water distribution across the cathode catalyst layer

In this section, the water distribution throughout the cathode catalyst layer is discussed. To avoid cluttering, the snap shot of the cathode catalyst layer for each certain iteration is depicted by the container, which represents the boundary of the cathode catalyst layer, and the location of water molecules only. The amount of hydroniums, oxygen molecules and water molecules that is still trapped inside the cathode catalyst layer is shown in other figures.

The simulation is started with the lowest input rate for hydronium and oxygen at three molecules per iteration and two molecules per iteration consecutively. As

hydroniums and oxygen molecules start to diffuse into the developed cathode catalyst layer, they are going to move and arrange themselves into a new configuration which has lower potential energy than the former configuration. Six water molecules will be created when four hydroniums and one oxygen molecule are in the same neighborhood. These processes will continue until the desired iteration is reached.
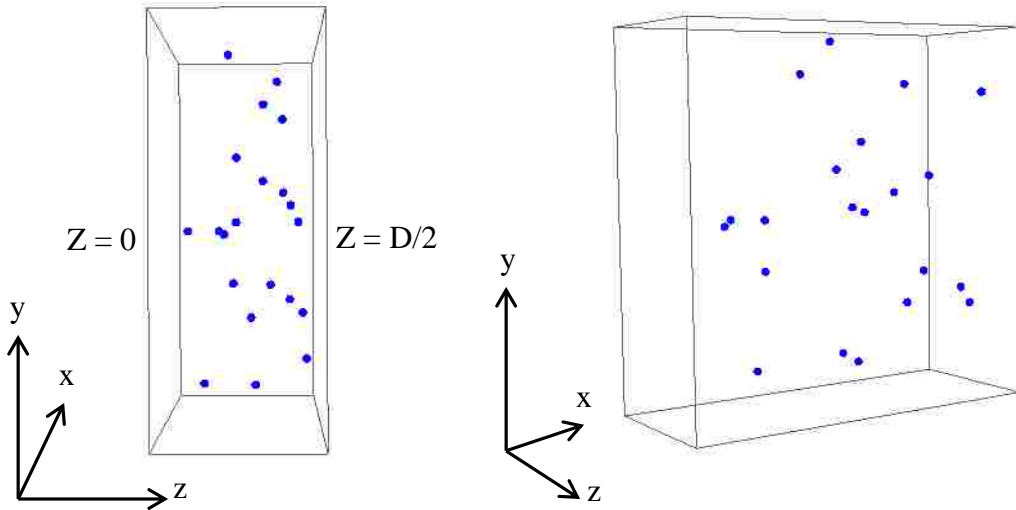
Figure 3.3. Simulation result at 1,000 iterations: Location of water molecules.

Figure 3.3 shows the snap shot of the cathode catalyst layer at 1,000 iterations. From this snap shot the newly-formed water molecules are located near the center of the cathode catalyst layer which can be explained by the movement of hydroniums and oxygen molecules. Molecular size of hydronium, oxygen and carbon are in the same range, 1.43 angstrom for hydronium, 1.5 angstrom for oxygen and 1.7 angstrom for carbon, then the movement of hydronium and oxygen tends to have the similar acceptance rate by this algorithm. Because of this reason, hydronium and oxygen tend to have the similar diffusivity rate thus, the location where the most electrochemical reaction has tendency to occur in the area where $\frac{Z}{D/2} = 0.5$. But from the potential constraint, each movement is possible if it goes to the lower potential energy level then

the newly formed water molecules tend to diffuse to the location where there are less

hydronium because the Lennard-Jones potential of hydronium-water is higher than the

Lennard-Jones potential of water-water and water-oxygen. As the hydronium

concentration is high at the location of $\frac{Z}{D/2} < 0.5$ then the newly formed waters tend to

diffuse to the location where $\frac{Z}{D/2} > 0.5$.

All of these explanations can be proved by the profiles of hydroniums, oxygen

molecules and water molecules which are shown in Figure 3.4. In this figure, 22% of

oxygen molecules are located in the area where $\frac{Z}{D/2} = 0.9$ and $\frac{Z}{D/2} = 0.1$ and another

17% and 21% of oxygen molecules are located at the location where $\frac{Z}{D/2} = 0.7$ and $\frac{Z}{D/2} =$

0.8 respectively. The majority of hydroniums can be found at the area where $\frac{Z}{D/2} < 0.3$

while most of the newly-formed water molecules are located in the area where $\frac{Z}{D/2} > 0.5$.
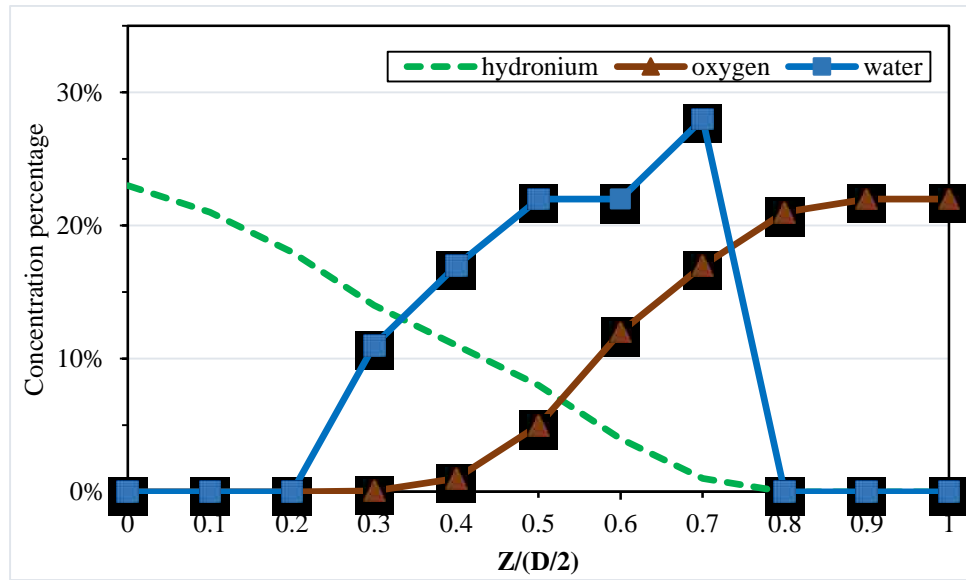
Figure 3.4. Simulation result at 1,000 iterations: Profiles of the hydroniums, and oxygen

and water molecules in the cathode catalyst layer.

54

Concentration percentage is the number of species at the individual location over the total

number of that species.

For the results of 5,000 iterations case are shown in Figure 3.5 and Figure 3.6.
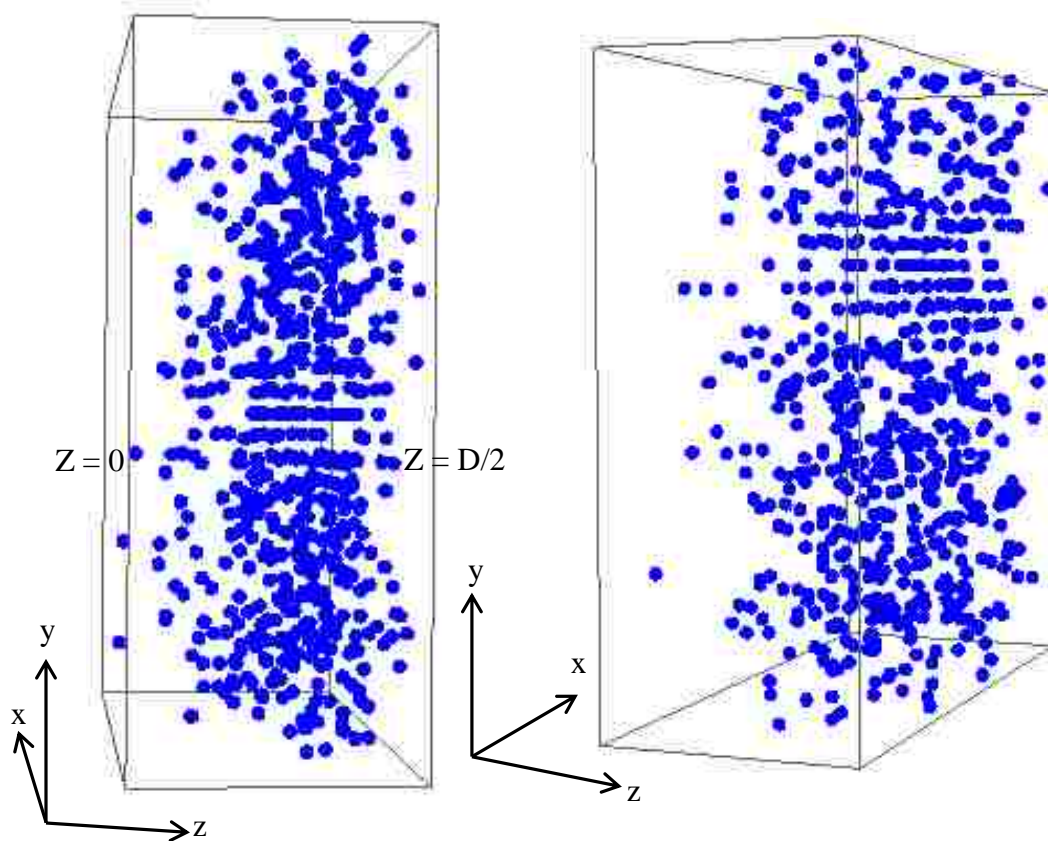
Figure 3.5. Simulation result at 5,000 iterations: location of water molecules.
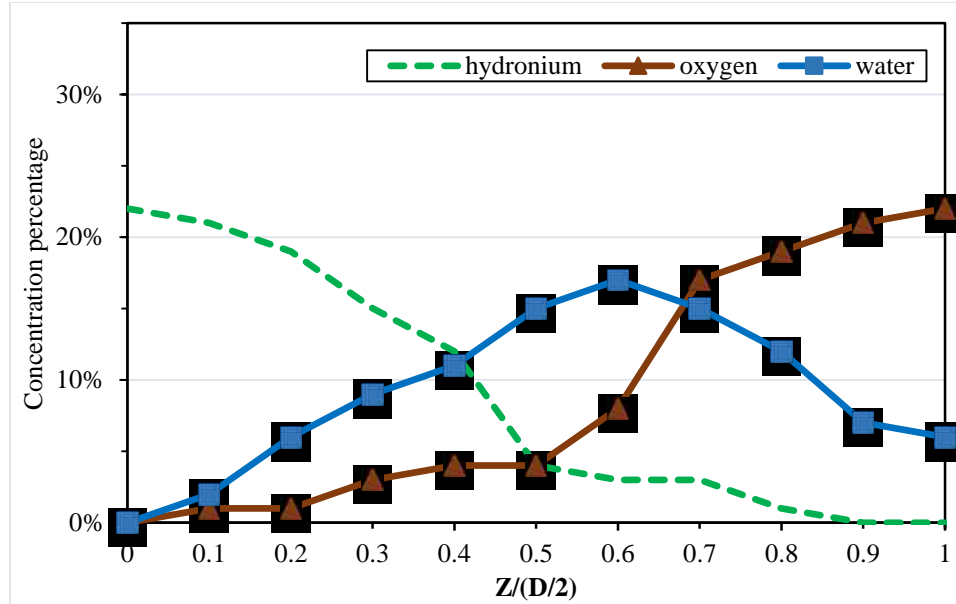
Figure 3.6. Simulation results at 5,000 iterations: Profiles of the hydroniums, and oxygen and water molecules in the cathode catalyst layer.

From Figure 3.5 and Figure 3.6, the majority of water molecules is located where $\frac{Z}{D/2} > 0.5$ while some of them can diffuse to the area where $\frac{Z}{D/2} < 0.5$ even though more oxygen molecules and hydroniums are allowed to enter into the developed cathode catalyst layer. This phenomenon can be explained by the following process.

(1) While this algorithm is continuously running, more water molecules will be formed in the cathode catalyst layer and they tend to move to the location where there are fewer hydroniums because the Lennard-Jones potential between water-hydronium is higher than the Lennard-Jones potential between water-oxygen. As the concentration of hydronium is higher at the location where $\frac{Z}{D/2} \to 0.3$ then water molecules will move in the opposite direction, the location where $\frac{Z}{D/2} >$

56

0.3, that is the reason of why water concentration is still high at the location where $\frac{Z}{D/2} > 0.5$.

(2) As more water molecules tend to move to the location where $\frac{Z}{D/2} > 0.5$, they will start to block the movement of oxygen molecules which make the oxygen molecules even harder to diffuse to the location where $\frac{Z}{D/2} \rightarrow 0$. Water molecules also block the movement of hydronium that try to diffuse to the location where $\frac{Z}{D/2} > 0.5$ that is the reason why the hydronium concentration is very high at the location of $\frac{Z}{D/2} < 0.5$.

(3) As water molecules and oxygen molecules started to accumulate near the location where $\frac{Z}{D/2} > 0.5$, water molecules themselves will try to diffuse to the new location in order to comply with the total potential energy constrain. Therefore, they start to migrate to the location of $\frac{Z}{D/2} < 1$ because there are fewer oxygen and water molecules in that location.

(4) Oxygen molecules also move similarly to the water molecules but their movements are more difficult than water because oxygen molecules have to pass through the cluster of newly-formed water and their movements could be possibly rejected due to the high Lennard-Jones potential. But some oxygen molecules can still move through the obstacle and locate themselves in the area where $\frac{Z}{D/2} \rightarrow 0.5$ as it can be found from the oxygen profile in Figure 3.6. These oxygen molecules will then have a chance to interact with hydroniums to form more water at this location.

While this algorithm is continuously running, hydroniums, oxygen and water molecules will follow these processes in order to minimize the total potential energy. Water molecules will start to diffuse through the cathode catalyst layer. As this algorithm is allowed to run to 15,000 iterations, the cathode catalyst layer is full of water molecules which can be seen in Figure 3.7.
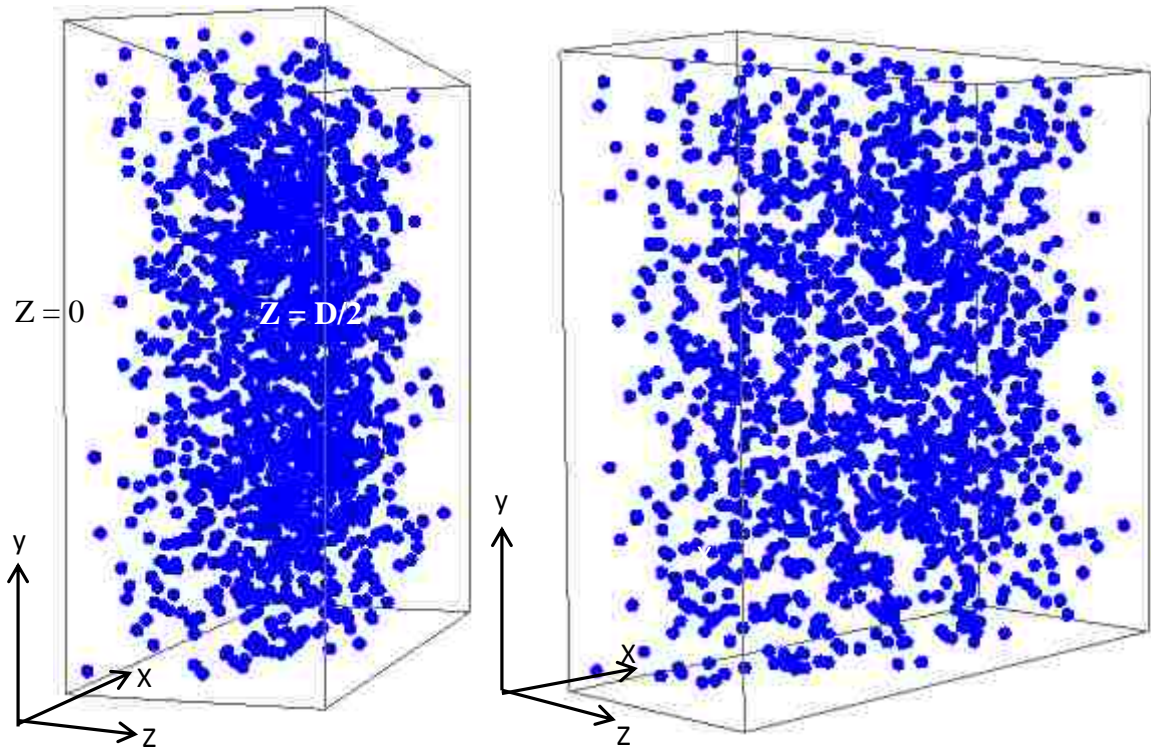
Figure 3.7. Simulation result at 15,000 iterations: Location of water molecules.

In this case, water molecules and oxygen molecules still behave in the similar way as they did in the 5,000 iterations case. But in the 15,000 iterations case, the large amount of water molecules that occupied the void space near $\frac{Z}{D/2} \to 1$ location have built up a potential wall and the movement of another water molecule that wants to diffuse to the $\frac{Z}{D/2} \to 1$ direction have been rejected because of the potential constraint then water molecules tended to diffuse to $\frac{Z}{D/2} \to 0$ direction instead. From the water profiles shown

in Figure 3.8, water molecules have already occupied the void space throughout the cathode catalyst layer. The movement of oxygen molecules is hindered by this water barrier but in the opposite way. As the oxygen concentration at the $\frac{Z}{D/2} \to 1$ location is very high then oxygen molecules will try to move to $\frac{Z}{D/2} \to 0$ direction but they are blocked by the water barrier and more oxygen molecules are stuck in this $\frac{Z}{D/2} \to 1$ location where the very high oxygen concentrations can be found.
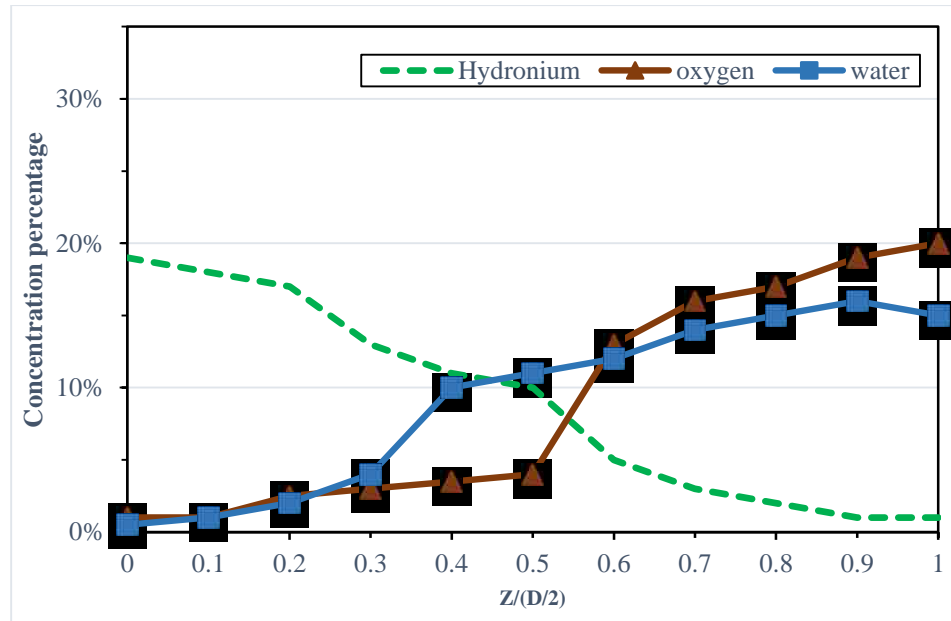

Figure 3.8. Simulation result at 15,000 iterations: Profiles of the hydroniums, and oxygen and water molecules in the cathode catalyst layer.

From Figure 3.8, the movement of hydronium is also affected by this water barrier. Hydronium needs a void space, which is already occupied by water molecules, to diffuse through this cathode catalyst layer. Thus, the hydronium concentration is higher at the area where $\frac{Z}{D/2} \to 0$. Very few hydroniums and oxygen molecules can diffuse

through the catalyst layer then the electrochemical reaction between these two species will hardly occur and this phenomenon will lead to the major loss for PEMFCs which called the concentration loss.

The number of hydroniums, oxygen molecules and water molecules that still located inside the cathode catalyst layer is shown in Table 3.1.

Table 3.1

Number of each species that located inside the cathode catalyst layer for each iterations

	Species		
Iteration	Hydronium	Oxygen	Water
1,000	2,815	1,932	24
5,000	3,528	2,231	634
15,000	2,694	1,788	1,923

From Table 3.1, it is clear to find that the number of each species that are still located inside the cathode catalyst layer does not follow the electrochemical reaction equation strictly. For 1,000 iterations the number of hydroniums and oxygen that enter in this developed catalyst layer is equal to 3,000 and 2,000 molecules, respectively, and the number of newly formed water molecules is equal to 24. If all newly formed water molecules are assumed to stay inside the developed cathode catalyst layer then the expected numbers of hydroniums and oxygen should equal to 2,984 and 1,996 molecules, respectively. But as shown in Table 3.1, the numbers of hydroniums and oxygen that still stay inside the developed catalyst layer are equal to 2,815 and 1,932 molecules, respectively. This means that some hydroniums and oxygen molecules have diffused out

of the developed catalyst layer which is possible because in this algorithm every species can move in any direction. When any of them move out of the developed catalyst layer, this algorithm will remove them from the memory array. Even though the number of each species that still stay inside the developed catalyst layer is not exactly equal to the expected number from the electrochemical reaction equation, the ratio of each species is still in a good agreement with the governing electrochemical reaction equation.

For 5000 and 15,000 iteration, the difference between the simulation result and the expected number from the electrochemical reaction equation is quite high and the reasons behind this phenomenon can be explained by the same explanation discussed in the previous.

3.3.2 The effect of hydronium and oxygen input

The effect of fuel input has been investigated by changing the input values of hydroniums and oxygen per iteration from three hydroniums and two oxygen molecules per iteration to five hydroniums and three oxygen molecules and finally six hydroniums and five oxygen molecules per iteration. The algorithm is allowed to run for 15,000 iterations for each fuel ratio and the number of each species that still locate inside the developed catalyst layer is compared to find the best fuel input ratio. Table 3.2 shows the result for each fuel input ratio.

Table 3.2

Number of each species for each fuel input ratio after 15,000 iterations

	Species		
Fuel input ratio	Hydronium	Oxygen	Water
3:2	2,694	1,788	1,923
5:3	2,467	1,644	2,281
6:5	2,240	1,327	2,653

From Table 3.2, the input ratio of 3:2 seems to be the best fuel input ratio for this simulation scenario because it shows the least amount of water molecules that is still trapped inside the catalyst layer. The input ration of 3:2 also gives the largest amount of oxygen molecules and hydronium which means the possibility for more electrochemical reactions is higher than another fuel input ratio. And it is found that as the number of input oxygen increases the number of trapped water molecules also increase which is not good for the performance for PEMFC because it can lead to a concentration loss and flooding problem.

This simulation simulates the diffusion and electrochemical reaction at the atomic level which gives the basic idea of how hydroniums and oxygen molecules react and form water molecules. This information can be transferred to macroscopic simulation model in order to create the practical modelling of the PEMFC or it can be coupled with the multiscale modeling which will be studied in the future research.

3.4 Conclusion

A Monte Carlo computational geometry algorithm which can simulate the electrochemical reaction inside the PEMFC cathode catalyst layer has been successfully developed. This algorithm controls the movement of reactants, which are hydroniums and oxygen molecules, and product water. These three species are allowed to interact and diffuse through the catalyst layer in which every movement is controlled by the Lennard-Jones potential. As the developed algorithm is allowed to run to 15,000 iterations it shows the phenomenon of the concentration loss due to a large amount of water molecules already occupied the void space in the cathode catalyst layer. The fuel input ratio is also investigated and the appropriate hydronium to oxygen ratio is equal to 3:2.

CHAPTER 4

THE EFFECT OF GAS CONTAMINATION AND METAL IMPURITY ON

THE PEMFC CATHODE CATALYST LAYER

4.1 Introduction

In Chapter 3, the electrochemical reaction between hydroniums and oxygen molecules and the movement of water, which is a product of this electrochemical reaction, have been investigated. Cathode catalyst layer (CCL) described in Chapter 3 is assumed to be made of 100% platinum coated carbon and the fuel input are pure hydroniums and oxygen molecules but in the real practice there are nothing as a perfect catalyst and pure fuel. Thus the material impurity and gas contamination must be considered in order to simulate the real working condition of the fuel cell.

There are three contamination and impurity sources for PEMFC which can be described as the following:

1. Hydrogen contamination: Hydrogen that has been used for the fuel cell usually comes from the reformation of the hydrocarbons or oxygenated hydrocarbons. Unfortunately there are some unavoidable impurities. The reformate or hydrogen rich gas which is produced from the steam reforming or autothermal reforming contains 70% hydrogen, 25% carbon dioxide, 2% carbon monoxide and another 3% of inert gas and sulfur [51].

2. Air (oxygen contamination): Oxygen is a fuel that is used to supply to the cathode side of the PEMFC and air, which typically contains 20.95% of oxygen [52], and this is the most practical fuel for the cathode side. But the

air pollutants with many impurities can flow into the cathode channel side of the PEMFC. NO_x, SO_x and CO_x are the undesired impurities that are always found in the PEMFC cathode catalyst layer and the percentage of these impurities varies with the air quality.

3. Other contamination: The last impurity found inside the PEMFC is the metallic ion impurity from a fuel cell component. The corrosion of any metallic part of the PEMFC such as flow field bipolar plates, inlet/outlet manifolds and cooling loops can introduce the Fe^{3+}, Ni^{2+}, Cu^{2+} and Cr^{3+} into the catalyst layer of the PEMFC [51].

Scholars have proposed studies of the contaminates' effect on the performance of fuel cell. Shi et al. [53] developed a model which investigated the effect of toluene, which is one of many volatile organic compounds found in the atmosphere, on the performance of fuel cell. In their model, the transient and steady state behaviors of the fuel cell were simulated which considered the oxygen reduction mechanism and contaminant reactions. From the result of their simulation, the contamination level of 750 ppb toluene yields a 48 mV performance drop at 1 Acm^{-2}. Their simulation results have been validated with experimental data on fuel cell toluene contamination at four different current densities (0.2, 0.5, 0.75, and 1 Acm^{-2}) and three toluene concentrations (1, 5, and 10 ppm).

Li et al. [54] studied the effect of toluene on PEMFC performance by changing the level of input toluene under different current densities. In their study, four different levels of toluene concentration were used as an input while they operated their fuel cell under five current densities. The result of this study showed that the cell performance

dropped immediately after the toluene was put into the air stream and the steady-state cell voltage drop is highly related to the toluene concentration. They also found that the relative humidity (RH) and cathode Pt loading is related to the performance of PEMFC. High RH and high Pt loading can help decrease the degradation of PEMFC. Another interesting result from this experiment is that the toluene contamination cannot be fully recovered because after the initial experiment they replaced the toluene contaminated air with a clean air but their fuel cell performance still steadily declined.

Li et al. [55] proposed the effect of cobalt (Co^{2+}) contamination on the performance of PEMFC. From this study they found that the concentration of cobalt highly affects the performance of PEMFC because the fuel cell voltage dropped significantly after the Co^{2+} was injected into the cathode air stream. It was observed for the low operating temperature, the effect of Co^{2+} contamination was more severe because the Pt surface tends to absorb more cobalt at the lower temperature.

Sun et al. [56] reported the performance loss of the iron-fed fuel cell which is another kind of fuel cell that can recover iron and electricity from acid mine drainage. From their study, the iron contamination occurs on both the electrode and membrane but the membrane contamination tends to show a more severe effect. The α-FeO(OH), which is the product from the iron-fed fuel cell, is the major source of the iron contamination and it needs to be pushed out from the membrane of the fuel cell before it can form the fouling layers on the surface of electrode. If the α-FeO(OH) successfully formed the fouling layer on the membrane it will increase the membrane electrical conductivity which will delay the electro-oxidation kinetic of the Fe^{3+} and lower the performance of the fuel cell.

Bouzek et al. [57] performed experiments to study the effect of mercury on the performance of PEMFC. Results from their experiment showed that mercury can cause a huge drop in the PEMFC's performance because it tends to be absorbed by the Pt coated catalyst and it is impossible to regenerate the Pt surface. Result from 7000 hours experiment, which was operated under the standard operation conditions, showed that an average contamination of mercury at the level of 10 μg N m^{-3} can decrease the performance of PEMFC by 20%.

Mohtadi et al. [58] showed that the poisoning rate of NO_2 is highly dependent on its concentration. With the supply of 5 ppm of NO_2, approximately 55% loss in current after 12 hours of exposure was observed. The performance of the cell can be recovered with the supply of neat air. However, full recovery cannot be obtainable after the repetitive poisoning. Cyclic voltammetry (CV) was performed to understand the contamination mechanism. Using the CV spectra of the cell before and after exposure to 5 ppm NO_2, they concluded that NO_2 is not catalytic surface poisoning, instead the ionomer and/or the catalyst ionomer interface could be affected by the exposure. From their experimental results, they hypothesized that NO_2 gets electrochemically reduced on the cathode. They also studied the effects of the concentration of NO_2 and found that the rate of poisoning is not a strong function of the NO_2 concentration.

Sulek et al. [59] proposed the effect of the metal ion contamination on the performance of PEMFC. They did a series of tests on four different types of metal ion and they found out the Al^{3+} has the worst effect on PEMFC's performance follow by Fe^{2+}, Ni^{2+} and Cr^{3+}. Results from these experiments also show that there is no change in the

performance of contaminated PEMFC until the membrane electrical conductivity loss was greater than approximately 15%.

Yang et al. [60] used a simulated NO_x/air mixture with a total concentration of NO and NO_2 (in a ratio of 9:1) ranging from 10 ppm to over 1000 ppm to investigate the degradation of the cell performance. Their experimental measurements indicated that the poisoning effect of NO_x is reversible with complete recovery being achieved over a very long time.

Chu et al. [61] developed a one-dimensional transient model to investigate the effects of CO on liquid water transport in the PEM fuel cell. Their results indicated that the saturation of liquid water is reduced in the catalytic layers. The distribution of liquid water depends more strongly on the CO concentration than on the dilution of hydrogen in the membrane electrode assembly (MEA) of the cell. Due to poisoning, the current density is reduced, weakening the effect of the electro-osmotic drag. Further, the oxygen reduction reaction is also suppressed, reducing the diffusion of water from the cathode to the anode. Much of the work has concentrated on understanding the effects of CO poisoning on the cell rather than a stack.

Even though there has been much research about the effect of the contamination on the performance of PEMFC, the mechanism and the electrochemical reaction that occur inside the cathode catalyst layer needs more study. This is needed to better understand the water transport phenomena which can lead to a more suitable approach for the water management in the PEMFC.

In this chapter the effect of metal impurity and gas contamination are studied by modifying the sphere packing algorithm developed in Chapter 2 to create the metal contaminated cathode catalyst layer. Also the electrochemical reaction algorithm described in Chapter 3 is modified to investigate the effect of gas contamination.

4.2 Numerical Simulation Algorithm

The numerical simulation approach described in Chapter 3 has been utilized again by separating the algorithm into two parts. The first part is the cathode catalyst layer formation using the sphere packing algorithm which includes metal impurity. The second part is the movement of hydroniums, oxygen, contamination gases (CO_2 and CO) and water through this developed cathode catalyst layer.

As described in the beginning of this chapter, metal impurities can occur in the cathode catalyst layer and aluminum and iron are selected to be the metal impurities in this study because they can greatly decrease the performance of the PEMFC. The metal impurities are also modeled as spheres while the radius of the metal sphere is equal to 1.94 angstrom [62] for iron and 1.84 angstrom [63] for aluminum. To create the impure cathode catalyst layer the sphere packing algorithm described in Chapter 3 is modified by adding these initial steps at the beginning of the sphere packing algorithm.

Step 1   Determine the desired percentage of the metal impurity which can vary from 0.25 wt % to 1 wt %. For an example if 0.25 wt% impurity is selected that means 25 out of 10,000 spheres are the metal impurities because the cathode catalyst layer is created from 10,000 spheres.

Step 2   Generate 3 random numbers and assign them as x, y and z to give the initial

coordinate of metal sphere and record this coordinate.

Step 3   Generate another 3 random numbers for the second coordinate of the metal

sphere.

Step 4   Test the coordinate from step (2) if the coordinate from step (2) is the same as

the coordinate from step (1) then repeat step (1) again, otherwise record this

coordinate.

Step 5   Repeat steps (3) and (4) until the number of desired metal spheres are placed in

the container.

The Lennard-Jones potential is used to control the potential energy of the sphere

packing process. For this case, iron and aluminum have been introduced in the packing

algorithm then the Lennard-Jones potential between carbon and iron and the Lennard-

Jones potential between carbon and aluminum must be considered. In order to determine

the Lennard-Jones parameter of carbon-iron and carbon-aluminum, the Lorentz/Berthelot

mixing rules described in Chapter 3 is utilized again.

For iron: σ_{ii} is equal to 2.32 angstrom and ε_{ii} is equal to 50.02 kJ per mol [64] and

for aluminum: σ_{jj} is equal to 2.62 angstrom and ε_{jj} is equal to 37.99 kJ per mol [64]. Then

the Lennard-Jones parameter for the mixes pair can be described as follows:

(1) Carbon-iron: σ_{ij} = 3.09 angstrom, ε_{ij} = 4.69 kJ per mol.

(2) Carbon-aluminum: σ_{ij} = 3.24 angstrom, ε_{ij} = 4.09 kJ per mol.

Figure 4.1 shows the example of 0.25 wt% iron impurity and these iron spheres

are randomly placed in the rectangular container. After being successfully placed, these

iron spheres do not move and the sphere packing algorithm described in Chapter 3 is allowed to run. The carbon spheres then interact with the metal impurity which results in the change of the cathode catalyst layer's structure compared to the pure carbon structure.
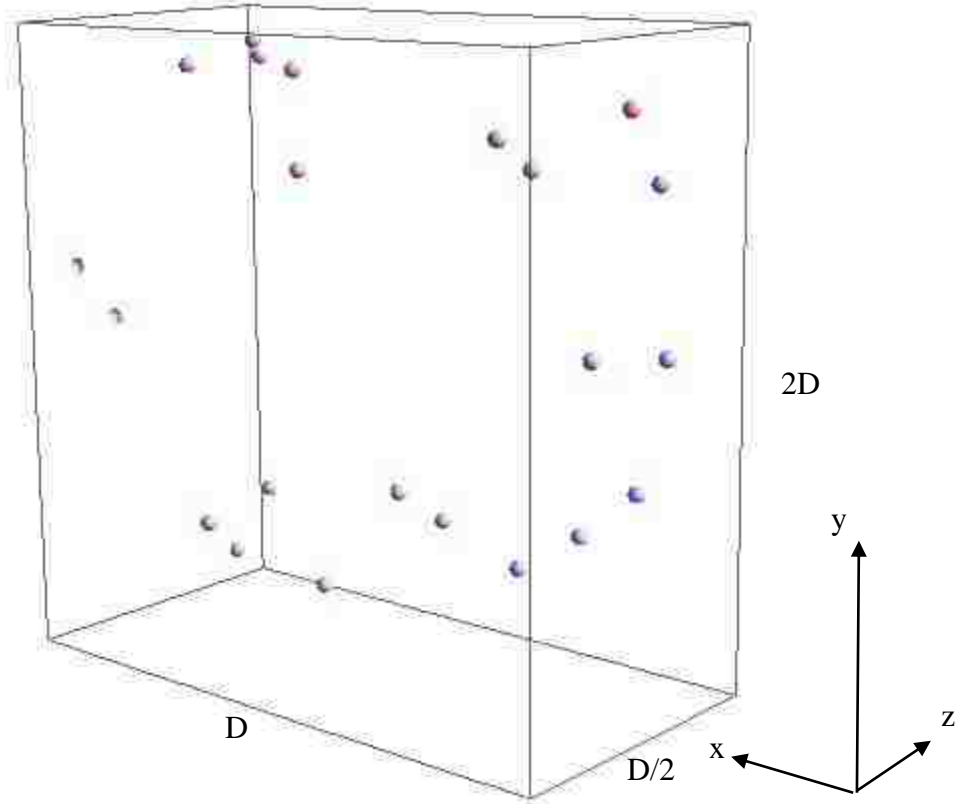
Figure 4.1. The example of randomly placed metal impurity inside CCL.

The sphere packing algorithm is allowed to run for 20 times for each level of impurity and the average solid fraction of each contamination percentage is calculated and listed in Table 4.1.

Table 4.1

The average solid fraction value with the different levels of impurity

	Average solid fraction value				
Impurity type/percentage	0%	0.25%	0.5%	0.75%	1%
Iron	0.611	0.604	0.592	0.587	0.574
Aluminum	0.611	0.607	0.602	0.591	0.583

From Table 4.1 it is clear to find that iron impurity has a greater effect on the carbon packing than the aluminum impurity which can be explained by the potential constraint. The Lennard-Jones potential between carbon-iron is higher than the Lennard-Jones potential between carbon-aluminum and the objective function of this sphere packing algorithm is to minimize the total potential energy of the system. Carbon spheres tend to be placed further away from the iron spheres in order to minimize the total potential energy. Thus, this packing configuration created a larger void space than the pure carbon configuration and carbon-aluminum configuration.

From the solid fraction values shown in Table 4.1, the developed cathode catalyst layer with the iron impurity is less dense than any other type of configuration. The less dense cathode catalyst layer allows more hydroniums, oxygen molecules, contamination gases and water molecules to diffuse into the catalyst layer. The effect of these metal impurities is discussed in the next section.

After the cathode catalyst layer is developed, the diffusion algorithm described in Chapter 3 is allowed to run. But in this chapter contamination gases are introduced to the

developed catalyst layer which means that the diffusion algorithm described in Chapter 3 needs to be modified. The modified algorithm can be described as follows:

Step 1   Randomly generate the initial location of hydroniums and oxygen molecules, the initial location of hydroniums will have the coordinate of (x , y , 0) and oxygen molecules will have the initial coordinate of (x , y , D/2) where x and y are random numbers.

Step 2   Check if the location of hydroniums, oxygen molecules and carbon molecules, from the sphere packing algorithm, overlap with each other or not. If there are no overlap then go to step (3) otherwise go back to step (1).

Step 3   Generate a random vector which has a magnitude of 0.5 x r_o, where r_o is the van der Waals radius of oxygen.

Step 4   Allow the oxygen number i to move along this vector.

Step 5   Test if the current coordinate of this oxygen overlaps with other molecules or not. If the current coordinate of oxygen number i overlaps with other molecules then go to back to step (3) otherwise go to step (6).

Step 6   Repeat steps (3-5) until all oxygen molecules have been moved and save this configuration as the new configuration.

Step 7   Calculate the total potential energy of this current configuration using the Lennard-Jones potential.

Step 8   Generate a random vector which has a magnitude of 0.5 x r_h, where r_h is the atomic radius of hydronium.

Step 9   Allow the hydronium number i to move along this vector.

Step 10   Test if the current coordinate of this hydronium overlaps with other molecules or not. If the current coordinate of hydronium number i overlaps with other molecules then go to back to step (8) otherwise go to step (11).

Step 11   Repeat steps (8-10) until all hydroniums have been moved and save this configuration as the current configuration.

Step 12   Calculate the total potential energy of this current configuration using the Lennard-Jones potential.

Step 13   Calculate the total potential energy difference between step (12) and step (7).

Step 14   If the total potential energy difference is less than zero then accepts the new configuration as current configuration and go to step (15) otherwise go back to step (8).

Step 15   Select the type of contaminate gas. It can be a carbon dioxide or a carbon monoxide and determine the percentage of the contaminate gas.

Step 16   For CO_2 the percentage can vary from 0.025 wt% for very clean air, to 0.04 wt% which is the average of the CO_2 concentration of the earth's atmosphere [65]. For CO, the percentage can vary from 0.0005 wt% to 0.0015 wt% which is the CO level from the vehicle exhaust [66].

The input amount for the contaminate gas per iteration is calculated from the relationship between the percentage of oxygen and the percentage of the contaminate gases. For an example, the oxygen concentration in the atmosphere is equal to 21% and the oxygen input per iteration equals two molecules but this simulation is going to run for 15,000 iterations then the total oxygen input is equal to 40,000 molecules. These 40,000 molecules are related to the 21% of the total gas in the atmosphere if the selected carbon dioxide percentage equals to 0.035 wt% then the total number of input carbon dioxide is equal to 67 molecules or 0.035 wt% of the total gas in the atmosphere. Because this simulation is allowed to run for 15,000 iterations but there are only 67 carbon dioxide molecules, so a single carbon dioxide molecule is introduced into the simulation system every 298 iterations. Table 4.2 shows the information of the input gas contamination.

Table 4.2

Gas contamination input for the simulation

Species	Weight percentage	Total amount	Iteration cycle for the contamination appearance
	0.0005	1	10,000
CO	0.001	2	6,667
	0.0015	3	5,000
	0.025	48	411
	0.03	57	344
CO_2	0.035	67	298
	0.04	76	259

Step 17   Randomly generate the initial location of contamination gas, the initial location

of this gas has the initial coordinate of (x, y, D/2) because the contamination gas

comes with air which is the source of oxygen input.

Step 18   Check if the location of hydroniums, oxygen molecules, carbon molecules and

contamination gas overlap with each other or not. If there is no overlap then go

to step (19) otherwise go back to step (17).

Step 19   Generate a random vector which has a magnitude of 0.5 x r_g, where r_g is the van

der Waals radius of the contamination gas. To define the radius of the

contamination gases, the following assumptions have been made.

(1) Contamination gases are in perfect spherical shape.

(2) For carbon dioxide, its sphere radius is equal to 1.16 angstrom as shown in

Figure 4.2.
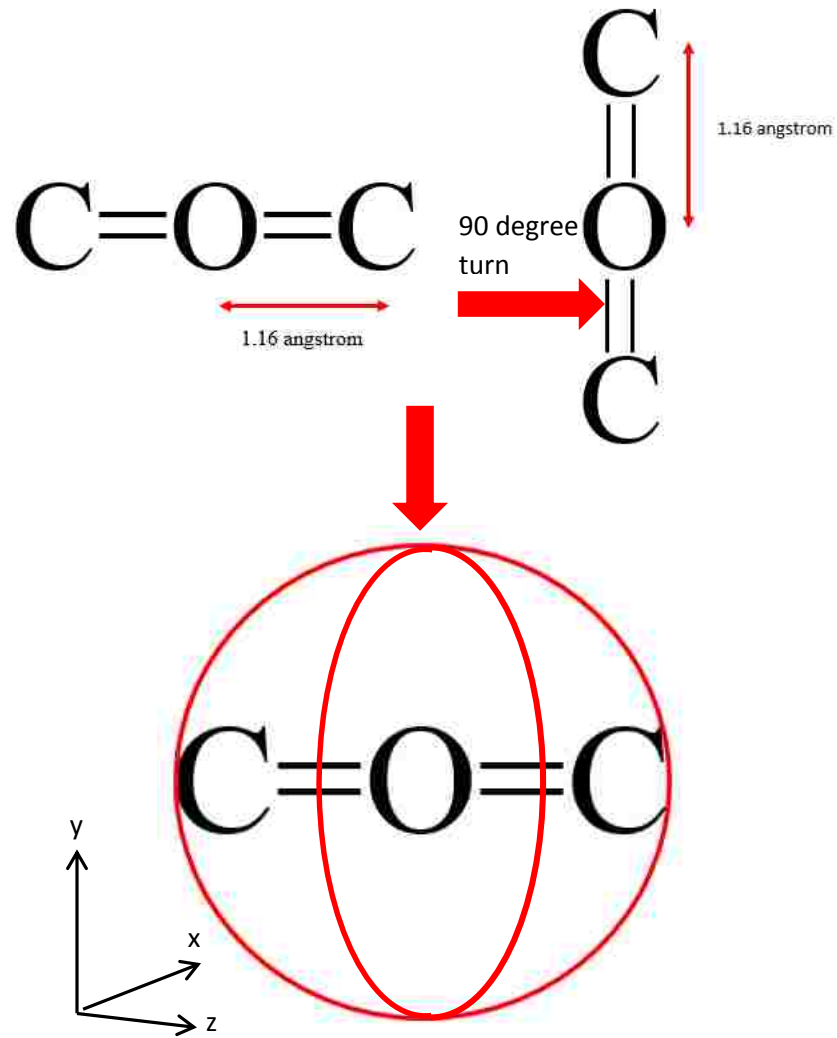
Figure 4.2. Carbon dioxide molecular radius.

From Figure 4.2, carbon dioxide has a linear bond shape with a length of 1.16 angstrom [67]. This bond can move or rotate in any direction and on any axis. If this carbon dioxide molecule rotates 90 degrees then it will occupy another space on top of its original location. When it does another 90 degrees rotation in the y, x and z directions it will occupy more space and that overall space will have a perfect spherical shape. That is the reason why the carbon dioxides in this simulation are all assumed to have a spherical shape.

(3) This concept also applied on the carbon monoxide too. This gas has only 1

triple bond and its bond length is equal to 1.12 angstrom [67]. Thus the

carbon monoxide sphere in this simulation is assumed to be a perfect sphere

with a 0.56 angstrom radius as shown in Figure 4.3.
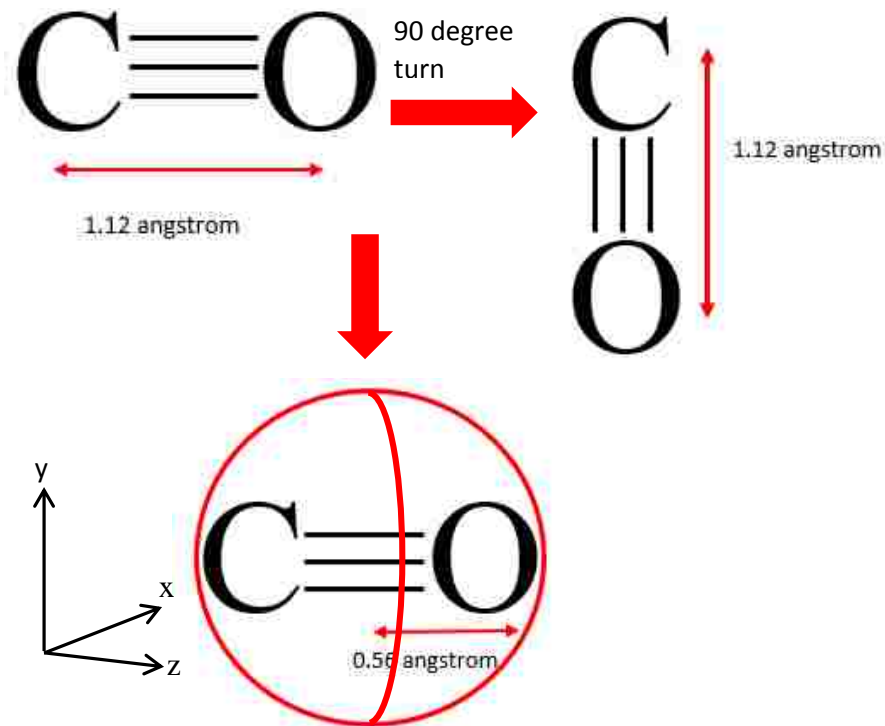
Figure 4.3. Carbon monoxide molecular radius.

Step 20   Allow contaminate gas molecule number *i* to move along this vector.

Step 21   Test if the current coordinate of this contaminate gas molecule overlaps with

other molecules or not. If the current coordinate of contaminate gas molecule

number *i* overlaps with other molecules then go to back to step (19) otherwise

go to step (22).

Step 22   Repeat steps (19-21) until all contaminate gas molecules have been moved and

save this configuration as the current configuration.

Step 23 Calculate the total potential energy of this current configuration using the Lennard-Jones potential. The full list of the Lennard-Jones parameters is shown in Appendix B.

Step 24 Calculate the total potential energy difference between step (24) and step (12).

Step 25 If the total potential energy difference is less than zero then accepts the new configuration as current configuration and go to step (26) otherwise go back to step (19).

Step 26 Check oxygen molecules number i if there are four hydroniums located within the length of 1 angstrom from the center of this oxygen molecule. If there are four hydroniums located within this length then a chemical reaction will happen. After this electrochemical reaction, six water molecules will replace those four hydroniums and oxygen molecule. The coordinate of these newly-formed water molecules will be at the center of the replaced hydroniums and oxygen. If there are no hydroniums within this 1 angstrom length then this algorithm will check oxygen molecules number $i+1$ for the possibility of this chemical reaction.

Step 27 Repeat step (26) until all oxygen molecules are tested.

Step 28 Generate a random vector which has a magnitude of 0.5 x r_w, where r_w is the van der Waals radius of water.

Step 29 Allow water number i to move along this vector.

Step 30 Test if the current coordinate of this water molecule overlaps with other

molecules or not. If the current coordinate of water number i overlaps with

other molecules then go back to step (17) otherwise go to step (18).

Step 31 Repeat steps (28-30) until all water molecules have been moved and save this

configuration as the new configuration.

Step 32 Calculate the total potential energy of this new configuration using the Lennard-

Jones potential.

Step 33 Calculate the total potential energy difference between step (32) and step (23).

Step 34 If total potential energy difference is less than zero then accepts the new

configuration as current configuration and go to step (35) otherwise go back to

step (28).

Step 35 Increase the number of iteration (t) by one and check the current value of the

iteration if it is still less than the desired iteration then go back to step (1)

otherwise stops. The flow chart of this algorithm is shown in Figure 4.4.
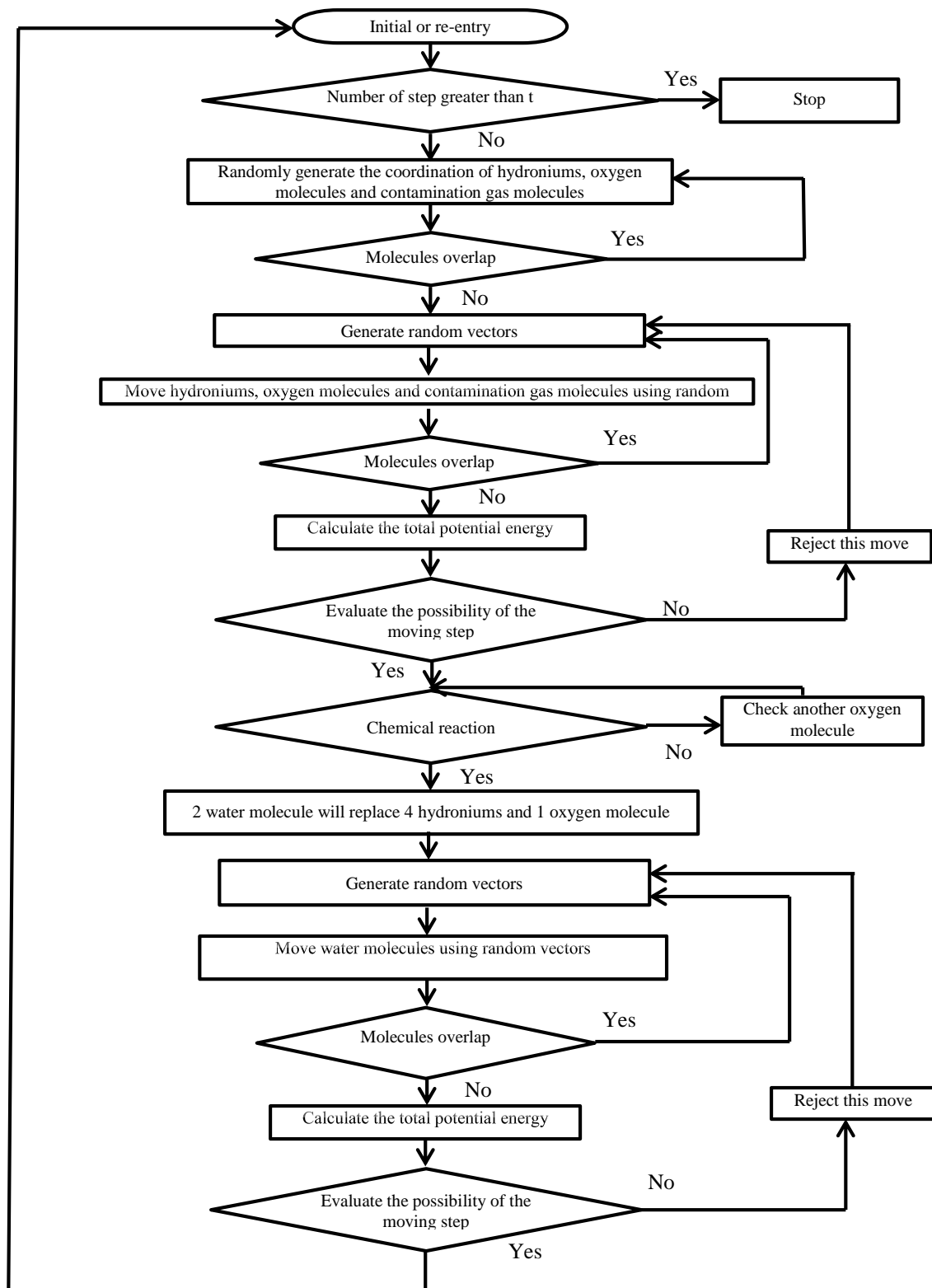
Figure 4.4. Flow chart of the developed algorithm with metal impurity and gas

contamination.

This developed algorithm is used to determine the effect of metal and gas contamination by changing the percentage of metal impurity in the developed cathode catalyst layer and the percentage of the input contamination gas. Each level of contamination is simulated for 10 times and each simulation is allowed to run for 15,000 iterations. The average amount of every species that still located inside the cathode catalyst layer is counted and the amount of newly formed water during these iterations is also recorded.

4.3 Results and Discussion

In this section the effect on the metal impurity and gas contamination are investigated based on the assumption that carbon monoxide and carbon dioxide are not absorbed on the platinum surface. The numerical simulation is started with the zero amount of metal impurity in the cathode catalyst layer. For each iteration, three hydroniums and two oxygen molecules are allowed to diffuse into this developed cathode catalyst layer and start the electrochemical reaction. Contaminate gas is also allowed to diffuse into this developed cathode catalyst layer and the amount of the contaminate gas per iteration is determined by the contaminate percentage. Only the intermolecular interaction among hydroniums, oxygen molecules, contaminate gases, metal impurities and product water is considered in this simulation.

After finishing the simulation with all desired percentage of gas contamination, the metal impurity is introduced into the cathode catalyst layer which resulted in the change of its structure. After that hydroniums, oxygen molecules and contaminate gas

are allowed to diffuse into this developed cathode catalyst layer again. The results of these simulation are shown in Table 4.3 to Table 4.12.

4.3.1 The effect of gas contamination

The effect of contaminate gases on the performance of 100% carbon cathode catalyst layer (CCL), created from 10,000 carbon spheres, is minimal as shown in Table 4.3. For CO contamination, the difference in the amount of newly formed water for 0% contamination and 0.0015% contamination is equal to 0.13% which is very small. The relationship between the contamination percentage and the amount of newly formed water is not clear because as the CO concentration increases from 0% to 0.0005% the amount of newly formed water decreases. But when the CO concentration increases from 0.0005% to 0.001%, the amount of newly formed water is also increased.

The similar phenomenon also happens with the CO_2 contamination case. The difference between the amount of newly formed water for 0% and 0.04% contamination concentration is only 0.41% and there is no clear relationship or evidence between the concentrations of CO_2 and the amount of newly formed water.

This phenomenon can be explained by the concentration of CO and CO_2 and the maximum iteration of this simulation. CO concentration is varied from 0% to 0.0015% and the concentration for CO_2 is varied from 0% to 0.04%, the total amount of the contamination gases that introduced into the system is very small compared to the amount of hydronium and oxygen molecule. Even though, the contaminate gas can interfere with the movements of hydronium and oxygen but the number of these contamination gases is too small to cause any significant effect on the system.

83

Table 4.3

The effect of gas contamination on 100% carbon CCL, created from 10,000 carbon

spheres

Type of gas contamination	Contamination percentage	Newly formed water (molecules)	Number of molecules after 15,000 iterations		
			hydronium	oxygen	water
CO	0	3,879	2,694	1,788	1,923
	0.0005	3,883	2,690	1,803	1,917
	0.001	3,882	2,687	1,796	1,924
	0.0015	3,877	2,695	1,793	1,920
CO_2	0	3,879	2,701	1,788	1,923
	0.025	3,888	2,686	1,796	1,935
	0.03	3,886	2,688	1,799	1,926
	0.035	3,890	2,676	1,791	1,935
	0.04	3,888	2,667	1,800	1,934

4.3.2 The effect of iron impurity

For 0.25 wt% iron impurity, the average amount of newly formed water is 1.84%

lower than the 100% carbon cathode catalyst layer case while the amount of water

molecules that still trapped inside the cathode catalyst layer after 15,000 iterations is

3.32% lower. The reason of why this simulation yields the lower amount of newly

formed water than the 100% carbon case is because iron is presented in the cathode

catalyst layer. From the spheres packing results shown in Table 4.1, structure of the

contaminated cathode catalyst layer is less dense than the non-contaminate one and this

less dense structure allows more hydroniums and oxygen molecules to diffuse deeply

inside its structure. When hydroniums and oxygen molecules move closer to the iron spheres they are all pushed away from their current position.

As iron spheres are randomly placed through the developed cathode catalyst layer then every move of hydroniums and oxygen molecules is highly to be rejected by the diffusion algorithm because the Lennard-Jones potential between hydronium-iron and oxygen-iron is much higher than the Lennard-Jones potential between hydronium-carbon and oxygen-carbon. Thus, hydroniums and oxygen molecules are forced to place themselves far away from iron spheres which make hydronium and oxygen molecule to be highly scattered throughout the cathode catalyst layer.

As described in Chapter 3, the electrochemical reaction in this algorithm happens when four hydroniums and two oxygen molecules share the same neighborhood but the presence of iron spheres in the cathode catalyst layer has reduced the possibility of the electrochemical reaction occurrence. In Table 4.4, the total amount of newly formed water for the 0.25 wt% iron impurity case is 1.84% lower than the 100% carbon catalyst case. There are only 25 iron spheres in the developed cathode catalyst layer and this amount is not enough to scatter the large amount of hydronium and oxygen molecules, thus the occurrence of electrochemical reaction for this 0.25 wt% iron impurity case is still very close to the 100% carbon catalyst case.

The amount of water that is still trapped inside the contaminated cathode catalyst is also lower than the non-contaminated one. It is because of a high Lennard-Jones potential between iron and water, 5.7 kJ per mol. To minimize the total potential energy, the developed algorithm has been tried to place water molecules away from iron spheres as much as possible which results in the diffusion of water molecules from the cathode

catalyst layer. But as described before, the amount of iron spheres is not large enough to cause a significant effect. That is the reason the amount of water that is still trapped inside the contaminated cathode catalyst layer is just 3.32% lower than the non-contaminated catalyst.

Table 4.4

The effect of metal impurity on CCL, created from 10000 spheres, with 0.25 wt% iron impurity

Type of gas contamination	Contamination percentage	Newly formed water (molecules)	Number of molecules after 15,000 iterations		
			hydronium	oxygen	water
CO	0	3,796	2,748	1,839	1,877
	0.0005	3,813	2,747	1,864	1,848
	0.001	3,835	2,742	1,862	1,826
	0.0015	3,800	2,747	1,847	1,859
CO_2	0	3,813	2,756	1,870	1,848
	0.025	3,839	2,741	1,872	1,882
	0.03	3,805	2,740	1,870	1,872
	0.035	3,820	2,725	1,863	1,879
	0.04	3,802	2,711	1,877	1,872

When the iron concentration in the developed cathode catalyst layer is increased to 0.5 wt%, the solid fraction value of the catalyst layer is reduced to 0.592 which means that there is more void space inside this developed cathode catalyst layer. Hydroniums and oxygen molecules can now easily diffuse into this catalyst layer but the presence of more iron spheres in the structure make these diffusions to be more scattering. This is the reason why the amount of newly formed water for this case is 4.66% lower than the

100% carbon case. Even though the higher percentage of iron impurity has reduced the occurrence of the electrochemical reaction, it does reduce the amount of water that still trapped inside the cathode catalyst layer by 8.98%. This lower amount of water can increase the lifetime of the cathode catalyst layer and the result of this simulation can be found in Table 4.5.

Table 4.5

The effect of metal impurity on CCL, created from 10000 spheres, with 0.5 wt% iron

impurity

Type of gas contamination	Contamination percentage	Newly formed water (molecules)	Number of molecules after 15,000 iterations		
			hydronium	oxygen	water
CO	0	3,728	2,775	1,860	1,765
	0.0005	3,704	2,767	1,868	1,739
	0.001	3,712	2,772	1,870	1,759
	0.0015	3,719	2,798	1,865	1,744
CO$_2$	0	3,681	2,778	1,847	1,752
	0.025	3,742	2,788	1,861	1,772
	0.03	3,681	2,797	1,874	1,720
	0.035	3,675	2,767	1,866	1,773
	0.04	3,698	2,763	1,870	1,758

For 0.75 wt% iron impurity, the higher percentage of iron impurity has reduced the amount of newly formed water by 6.59% and the amount of water molecule that is still trapped inside the cathode catalyst layer is reduced by 11.64% as shown in Table 4.6.

Table 4.6

The effect of metal impurity on CCL, created from 10000 spheres, with 0.75 wt% iron

impurity

Type of gas contamination	Contamination percentage	Newly formed water (molecules)	Number of molecules after 15,000 iterations		
			hydronium	oxygen	water
CO	0	3,619	2,804	1,833	1,694
	0.0005	3,638	2,805	1,842	1,686
	0.001	3,606	2,794	1,835	1,709
	0.0015	3,618	2,807	1,828	1,692
CO$_2$	0	3,642	2,813	1,826	1,706
	0.025	3,605	2,791	1,840	1,705
	0.03	3,642	2,800	1,835	1,705
	0.035	3,641	2,787	1,837	1,711
	0.04	3,650	2,777	1,848	1,714

The highest iron concentration for this study is equal to 1 wt%. For this iron concentration, there are 100 iron spheres embedded in the cathode catalyst layer based on 10,000 spheres configuration. These iron spheres show some effects on the electrochemical reaction and water transport phenomena inside the developed cathode catalyst layer. These iron spheres not only reduce the amount of newly formed water by 12.13% but also lower the number of water molecules that is still trapped inside the catalyst layer by 14.54%. The simulation results are shown in Table 4.7.

Table 4.7

The effect of metal impurity on CCL, created from 10000 spheres, with 1 wt% iron

impurity

Type of gas contamination	Contamination percentage	Newly formed water (molecules)	Number of molecules after 15,000 iterations		
			hydronium	oxygen	water
CO	0	3,421	2,751	1,849	1,636
	0.0005	3,378	2,757	1,868	1,617
	0.001	3,381	2,750	1,848	1,653
	0.0015	3,426	2,747	1,861	1,634
CO$_2$	0	3,421	2,756	1,842	1,648
	0.025	3,434	2,748	1,865	1,683
	0.03	3,408	2,760	1,858	1,643
	0.035	3,462	2,727	1,853	1,641
	0.04	3,393	2,728	1,869	1,661

From Table 4.3 to Table 4.7, it is found that the iron concentration is inversely proportional to the amount of newly formed water and the number of water molecules that is still trapped inside the cathode catalyst layer. These two factors are directly related to the performance of the PEMFC, the amount of newly formed water indicates the electrical power output and the number of water molecules that is still located inside can determine the lifetime of the cathode catalyst layer. In order to maintain the performance of the PEMFC, these water variables must be managed carefully. The amount of newly formed water should be as high as possible while keeping the number of water molecules inside the cathode catalyst layer at the minimal level.

The ratio of the amount of newly formed water to the number of water molecules that is still trapped inside the cathode catalyst layer can be the indicator for the performance of the fuel cell. A PEMFC that has good performance is supposed to have a high water ratio. The value of this water ratio from the iron impurity simulation, based on the 10000 spheres cathode catalyst layer, is calculated and listed in Table 4.8.

Table 4.8

The average water ratio for each iron impurity percentage

Impurity weight percentage	A: The average amount of newly formed water (molecule)	B: The average number of water molecule trapped inside the CCL	Water ratio (A/B)
0	3,885	1,926	2.02
0.25	3,814	1,862	2.05
0.5	3,704	1,753	2.11
0.75	3,629	1,702	2.13
1	3,414	1,646	2.07

Because the effect from the gas contamination is very small then the average value of newly formed water and the number of water molecules that is trapped inside the cathode catalyst layer is calculated regardless of the gas contamination. From Table 4.8, the water ratio of the 0.75 wt% iron impurity which equals to 2.13 is the highest compared to other iron impurity percentages which means that this 0.75 wt% iron impurity is the most appropriate amount of impurity in the material preparation. Even though the pure carbon catalyst yields the largest amount of newly formed water or on the other hand it gives the maximum electrical power output, it also yields the maximum

the number of water molecules that is still trapped inside the cathode catalyst layer which results in the poor lifetime of the catalyst layer.

For the 0.75 wt% iron impurity, the average number of water molecules that trapped inside the cathode catalyst layer is 11.64% lower than that of the pure carbon catalyst layer which means that the lifetime of this impure catalyst layer is longer. However, this impure catalyst layer has to sacrifice the electrical power output in order to perform at the long time because the average amount of newly formed water for this 0.75 wt% iron impurity is 6.59% lower than the pure carbon catalyst case.

4.3.3 The effect of aluminum impurity

From Table 4.1, the cathode catalyst layer structure with the aluminum impurity is denser than that with the iron impurity then the amount of hydroniums, oxygen molecules and gas contamination that diffused into this aluminum contaminated cathode catalyst layer are supposed to be less. If less hydroniums and oxygen molecules are diffused into the developed cathode catalyst layer then the possibility for the occurrence of electrochemical reaction should be lower but this the numerical simulation results in Table 4.9 to Table 4.12 show the opposite result. At the level of 0.25% impurity as shown in Table 4.9, the average amount of newly formed water is just 1.54% less than the 100% carbon catalyst case and the number of water molecules that still trapped inside this cathode catalyst layer is just 1.15% less than the pure carbon catalyst. This phenomenon can be explained by the mixed pair Lennard-Jones potential. The mixed pair Lennard-Jones potential of aluminum and other species are less than that of the iron, so less molecule scatter can be expected. And also for 0.25% impurity, the number of aluminum molecule that is embedded in the developed catalyst layer is just 25 molecules

which is too small to scatter the large amount of hydroniums and oxygen molecules, so the transport phenomenon inside this catalyst layer is quite similar to the pure carbon catalyst layer.

Table 4.9

The effect of metal impurity on CCL, created from 10000 spheres, with 0.25 wt% aluminum impurity

Type of gas contamination	Contamination percentage	Newly formed water (molecules)	Number of molecules after 15,000 iterations		
			hydronium	oxygen	water
CO	0	3,809	2,778	1,831	1,904
	0.0005	3,840	2,779	1,847	1,903
	0.001	3,823	2,783	1,839	1,903
	0.0015	3,822	2,773	1,837	1,907
CO_2	0	3,830	2,786	1,832	1,896
	0.025	3,826	2,791	1,839	1,904
	0.03	3,816	2,779	1,843	1,894
	0.035	3,816	2,775	1,834	1,922
	0.04	3,844	2,760	1,844	1,905

For 0.5 wt% aluminum impurity, the transport phenomena inside the developed cathode catalyst layer are similar to the 0.5 wt% iron impurity case but the hydronium and oxygen scatters are not as big as the scatter pattern that occurred in the iron contaminated catalyst. Compared to 0.5 wt% iron impurity case, more water molecules

are formed in this catalyst layer but less water has been repelled out of it. From Table 4.10, the average amount of newly formed water is equal to 3,750 molecules or 3.47% lower than that of the pure carbon catalyst layer while the average number of water molecule inside this catalyst layer equals to 1,804 or 6.36% lower than the average amount of water that still trapped inside the 100% carbon catalyst.

Table 4.10

The effect of metal impurity on CCL, created from 10000 spheres, with 0.5 wt% aluminum impurity

Type of gas contamination	Contamination percentage	Newly formed water (molecules)	Number of molecules after 15,000 iterations		
			hydronium	oxygen	water
	3,763	2,752	1,849	1,796	3,763
	3,759	2,751	1,864	1,785	3,759
CO	3,750	2,745	1,857	1,809	3,750
	3,748	2,754	1,854	1,801	3,748
	3,732	2,763	1,849	1,811	3,732
	3,745	2,753	1,857	1,804	3,745
CO_2	3,754	2,743	1,860	1,808	3,754
	3,761	2,733	1,852	1,804	3,761
	3,743	2,727	1,861	1,816	3,743

Table 4.11 shows the simulation results for 0.75 wt% aluminum impurity. For this case, the average amount of newly formed water is equal to 3,723 molecules or

4.18% lower than the pure carbon case and the number of water molecules inside this cathode catalyst equals to 1,768 molecules or 8.23%.

Table 4.11

The effect of metal impurity on CCL, created from 10000 spheres, with 0.75 wt% aluminum impurity

Type of gas contamination	Contamination percentage	Newly formed water (molecules)	Number of molecules after 15,000 iterations		
			hydronium	oxygen	water
CO	0	3,724	2,803	1,826	1,769
	0.0005	3,693	2,809	1,845	1,764
	0.001	3,723	2,810	1,837	1,768
	0.0015	3,740	2,809	1,832	1,757
CO$_2$	0	3,732	2,820	1,824	1,758
	0.025	3,698	2,794	1,835	1,780
	0.03	3,723	2,801	1,852	1,767
	0.035	3,769	2,787	1,838	1,779
	0.04	3,704	2,781	1,840	1,770

For the 1 wt% aluminum impurity, the average amount of newly formed water is equal to 3,593 molecules or 7.52% lower than the pure carbon case and the number of water molecules inside this cathode catalyst equals to 1,702 molecules or 11.67% which is shown in Table 4.12.

Table 4.12

The effect of metal impurity on CCL, created from 10000 spheres, with 1 wt% aluminum

impurity

Type of gas contamination	Contamination percentage	Newly formed water (molecules)	Number of molecules after 15,000 iterations		
			hydronium	oxygen	water
CO	0	3,607	2,751	1,862	1,708
	0.0005	3,580	2,760	1,880	1,698
	0.001	3,587	2,754	1,881	1,703
	0.0015	3,604	2,755	1,876	1,684
CO$_2$	0	3,580	2,771	1,865	1,704
	0.025	3,592	2,754	1,870	1,695
	0.03	3,583	2,752	1,886	1,701
	0.035	3,590	2,733	1,872	1,707
	0.04	3,611	2,730	1,874	1,715

In order to determine the amount of aluminum impurity that shows a positive effect on the performance of this catalyst layer, the ratio of newly formed water to the number of water molecules that still trapped inside the catalyst layer, based on 10000 spheres catalyst layer, for each level of aluminum impurity is calculated which can be found in Table 4.13.

Table 4.13

The average water ratio for iron and aluminum impurity

Impurity type	Impurity weight percentage	A: The average amount of newly formed water (molecule)	B: The average number of water molecule inside the CCL	Water ratio (A/B)
Iron	0	3,885	1,926	2.02
	0.25	3,814	1,862	2.05
	0.5	3,704	1,753	2.11
	0.75	3,629	1,702	2.13
	1	3,414	1,646	2.07
Aluminum	0	3,885	1,926	2.02
	0.25	3,825	1,904	2.01
	0.5	3,750	1,804	2.08
	0.75	3,723	1,768	2.10
	1	3,593	1,702	2.11

In Table 4.13, the aluminum concentration of 1 wt% yields the highest value of water ratio compared to other percentages of aluminum impurity however the iron impurity of 0.75 wt% is still the best impurity level for the PEMFC because it gives the highest water ratio value.

From all of the information found above, the embedded metal impurity in the PEMFC cathode catalyst layer is a good approach for PEMFC water management because the metal impurity, especially iron, can help decrease the amount of water inside the cathode catalyst layer which can extend the lifetime of the PEMFC. But this approach also has the drawbacks which are (1) the decrement of electrical power output

from the PEMFC (2) construction of the desired impure cathode catalyst layer is quite difficult to achieve because the catalyst production processes cannot control the randomness of the metal embedded and the impurity percentage may not be at the exact level as anticipated.

4.4 Conclusion

In this chapter, the effects of gas and metal impurity have been studied by modifying the sphere packing algorithm described in Chapter 2 and Chapter 3 to create the contaminated cathode catalyst layer. Also the diffusion and electrochemical reaction algorithm from Chapter 3 is modified to simulate the effect of gas contamination.

From the numerical simulation results, the effect of the gas contamination is minimal because the number of contamination gas molecules is too small and this simulation is a transient state simulation. Unlike the gas contamination, the metal impurity has the significant effect on the performance of the cathode catalyst layer. For 0.25 wt% iron impurity, it can decrease the amount of newly formed water by almost 2% and the number of water molecules that is still trapped inside the cathode catalyst layer after 15,000 iterations is decreased by 3.32% compared to the pure carbon catalyst. The amount of newly formed water and the number of water molecules trapped inside the cathode catalyst layer decrease as the metal impurity percentage increase. Iron impurity seems to have more positive effects on the performance of PEMFC because the ratio of the amount of newly formed water to the number of water molecule inside the catalyst for iron impurity is higher than that of the aluminum impurity. The 0.75 wt% iron impurity shows the most positive effect on the performance of PEMFC because it yields the highest water ratio of 2.13.

CHAPTER 5

CONCLUSIONS AND RECOMMENDATIONS

5.1 Conclusions

The objective of this work is to find the effective approach to manage water inside the cathode catalyst layer. To achieve this objective, the transport phenomena and the electrochemical reaction inside the cathode catalyst layer are simulated at the atomic scale. The first task for this work is to simulate a porous media structure that can represent the cathode catalyst layer. An optimization technique called ARSET coupled with the self-developed sphere packing algorithm is used to create this porous media. The ARSET algorithm which can vary the magnitude of the random vector helps to reduce the processing of sphere packing algorithm by 34% while the sphere packing results are in a good agreement with the previous publications. This study has been published in the Journal of Advanced Powder Technology (Volume 24, Issue 6, November 2013, Pages 955-961).

The second task for this work was to simulate the movement and the electrochemical reaction of hydroniums and oxygen molecules and also the diffusion of water which is a product of this electrochemical reaction. A Monte Carlo algorithm is again used for this study and the simulation is run for 1000, 5000 and 15000 iterations to investigate the distribution of these three species throughout the developed cathode catalyst layer. At 15,000 iterations, this developed cathode catalyst layer shows phenomena of the concentration loss because water molecules already occupied most of the void space in the catalyst layer. Another parameter that has been investigated in this

study is the ratio of hydronium and oxygen input and the result of this simulation shows that the fuel input ratio of 3:2 is the most appropriate ratio because it shows the least amount of water molecules that are still trapped inside the cathode catalyst after the end of simulation. This study is submitted to the Journal of Power Source, and it is under the review process.

The algorithms from the first and second task are modified again to simulate the effects of gas contamination and metal impurity. CO and CO_2 are selected to be the gas contaminants while the metal impurities are iron and aluminum. In this study, gas contamination shows a very little effect on the catalyst layer because the contamination percentage of these gases is very small. However, the metal impurity shows a significant effect on the amount of newly formed water and the number of water molecules that still trapped inside the cathode catalyst layer after 15,000 iterations. Iron impurity shows a more positive effect on the performance of PEMFC than the aluminum impurity because it yields the higher ratio of the newly formed water to the amount of water molecules that still trapped inside the cathode catalyst layer than the aluminum impurity. This study is also submitted to the Journal of Power Source and it is under the review process.

5.2 Recommendations for Future Work

There are three suggestions for future work which are:

(1) The composition of the actual cathode catalyst layer are carbon and platinum then carbon and platinum molecules should be packed together. The platinum molecules are supposed to be attached to the surface of the carbon molecules and

allow the sphere packing algorithm to pack a number of these molecular pairs in the container.

(2) The movement of electrons through the cathode catalyst layer should be simulated. After electrons are conducted through the cathode catalyst layer, they will interact with hydroniums and oxygen molecules. If four hydroniums, four electrons and two oxygen molecules share the same neighborhood then six water molecules will appear and replace those molecules.

(3) The operating temperature should be considered and the thermodynamic properties of each species should be introduced in the simulation.

APPENDIX A

NOMENCLATURE

Symbol	Name	Unit
D	base side of the container	angstrom(Å)
r_c	radius of the carbon sphere	angstrom(Å)
N	number of spheres in the sphere packing algorithm	-
p	random number used to create the random vector	-
$L(r_{ij})$	the total Lennard-Jones potential energy of the system	kJ per mol
ε_{ii}	the Lennard-Jones potential for same specie interaction	kJ per mol
ε_{ij}	the Lennard-Jones potential for mixed pair interaction	kJ per mol
σ_{ii}	the finite distance at which the inter-particle Lennard-Jones potential of the same species is zero	angstrom(Å)
σ_{ij}	the finite distance at which the inter-particle Lennard-Jones potential of the mixed pair molecule is zero	angstrom(Å)
$M(r_{ij})$	the total Morse potential energy of the system	kJ per mol
α_{ii}	parameter which controls the width of Morse potential well	angstrom^{-1}(Å^{-1})
ε_m	the Morse potential parameter	kJ mol^{-1}Å^2
α	parameter which controls the width of random number pool	-
q	random number which controls the increment or decrement of the random vector's magnitude	-
σ	standard deviation	

APPENDIX B

THE LENNARD-JONES PARAMETERS

Mixed	Lennard-Jones parameters	
paired molecules	ε (kJ per mol)	σ (angstrom)
Carbon-carbon	0.44	3.85
Carbon-water	0.53	3.51
Carbon-hydronium	2.82	3.19
Carbon-oxygen	0.43	3.43
Carbon-CO	0.62	3.81
Carbon-CO_2	0.86	4.15
Carbon-iron	4.69	3.09
Carbon-aluminum	4.09	3.24
Water-water	0.65	3.17
Water-hydronium	3.42	2.84
Water-oxygen	0.53	3.08
Water-CO	0.76	3.46
Water-CO_2	1.04	3.80

Mixed	Lennard-Jones parameters	
paired molecules	ε (kJ per mol)	σ (angstrom)
Water-iron	5.70	2.74
Water-aluminum	4.97	2.89
Hydronium-hydronium	18.04	2.52
Hydronium-oxygen	2.78	2.76
Hydronium-CO	4.00	3.14
Hydronium-CO_2	0.91	3.92
Hydronium-iron	30.04	2.42
Hydronium-aluminum	26.18	2.57
Oxygen-oxygen	0.43	3.00
Oxygen-CO	0.62	3.38
Oxygen-CO_2	0.85	3.72
Oxygen-iron	4.64	2.66
Oxygen-aluminum	4.04	2.81
CO-CO	0.89	3.76
CO-CO2	1.22	4.10

Mixed	Lennard-Jones parameters	
paired molecules	ε (kJ per mol)	σ (angstrom)
CO-iron	6.66	3.04
CO-aluminum	5.81	3.19
CO_2-CO_2	1.67	4.44
CO_2-iron	9.15	3.38
CO_2-aluminum	7.98	3.53
Iron-iron	50.02	2.32
Iron-aluminum	43.59	2.47
Aluminum-aluminum	37.99	2.62

BIBLIOGRAPHY

[1] Wanga, K., Chen, S., Mishler, J., Cho, S.C., & Adroher, X.C. (2011). A review of
     polymer electrolyte membrane fuel cells: technology, applications, and needs
     on fundamental research. *Applied Energy*, 88(4), 981–1007.

[2] *Fuel Cells Thermodynamics*. Retrieve from Rutgers, The State University of New
     Jersey, Edward J. Bloustein School of Planning and Public Policy website:
     http://policy.rutgers.edu/ceeep/hydrogen/education/ThermodynamicsFuelCells.
     pdf

[3] Nguyen, T.V., & White, R.E. (1993). A water and heat management model for
     proton-exchange-membrane fuel cells. *Journal of the Electrochemical Society*,
     140(8), 2178-2186.

[4] Huang, W., Zhoun, B., & Sobiesiak, A. (2005). Along-channel mathematical
     modelling for proton exchange membrane fuel cells. *International Journal of
     Energy Research*, 29(12), 1051–1071.

[5] Weber, A.Z., & Newman, J. (2006). Coupled Thermal and Water Management in
     Polymer Electrolyte Fuel Cells. *Journal of the Electrochemical Society,*
     153(12), A2205-A2214.

[6] Dannenberg, K., Ekdunge, P., & Lindbergh, G. (2000). Mathematical model of the
     PEMFC. *Journal of Applied Electrochemistry*, 30(12), 1377-1387.

[7]   Fronk, M.H., Wetter, D.L., Masten, D.A., & Bosco, A. (2000). PEM Fuel Cell
      System Solutions for Transportation. *Fuel Cell Power for Transportation 2000,
      Proc. Of SAE 2000 World Congress*, 101-108.

[8]   Geyer, H.K., & Ahluwalia, R.K. (1998). GC Tool for Fuel Cell System Design and
      Analysis: User Documentation. Argonne National Labs, Report No. ANL-98/9.

[9]   Um, S., Wang, C.Y., & Chen, K.S. (2000). Computational Fluid Dynamics Model
      of PEM Fuel Cells. *Journal of the Electrochemical Society*, 147(12), 4485-
      4493.

[10] Shan, Y.Y., & Choe, S.Y. (2005). A high dynamic PEM fuel cell model with
      temperature effects. *Journal of Power Sources*, 145(1), 30-39.

[11] Haddad, A., Bouyekhf, R., Moudni, A.E. (2008). Dynamic modeling and water
      management in proton exchange membrane fuel cell. *International Journal of
      Hydrogen Energy*, 33(21), 6239-6252.

[12] Serincan, M.F., & Yesilyurt, S. (2007). Transient analysis of proton electrolyte
      membrane fuel cells (PEMFC) at start-up and failure. *Fuel Cells*, 7(2), 118-
      127.

[13] Li, A.D., & Zhou, B. (2008). A general model of proton exchange membrane fuel
      cell. *Journal of Power Sources*, 182(1), 197-222.

[14] Wang, Y., & Wang, C.Y. (2005). Transient analysis of polymer electrolyte fuel
      cells. *Electrochima Acta*, 50(6), 1307-1315.

[15] Shimpalee, S., Beuscher, U., & Van Zee, J.W. (2007). Analysis of GDL flooding effects on PEMFC performance. *Electrochima Acta*, 52(24), 6748-6754.

[16] Paquin, M., & Fréchette, L.G. (2008). Understanding cathode flooding and dry-out for water management in air breathing PEM fuel cells. *Journal of Power Sources*, 180(1), 440-451.

[17] Meng, H., & Wang, C.Y. (2005). New model of two-phase flow and flooding dynamics in polymer electrolyte fuel cells. *Journal of the Electrochemical Society*, 152(9), A1733-A1741.

[18] Lin, G.Y., He, W.S., & Nguyen, T.V. (2004). Modeling liquid water effects in the gas diffusion and catalyst layers of the cathode of a PEM fuel cell. *Journal of the Electrochemical Society*, 151(12), A1999-A2006.

[19] Liu, Z.X., Mao, Z.Q., & Wang, C. (2006). A two dimensional partial flooding model for PEMFC. *Journal of Power Sources*, 158(2), 1229-1239.

[20] Zhu, X., Sui, P.C., & Djilali, N. (2007). Dynamic behavior of liquid water emerging from a GDL pore into a PEMFC gas flow channel. *Journal of Power Sources*, 172(1), 287-295.

[21] Fouquet, N., Doulet, C., Nouillant, C., Dauphin-Tanguy, G., & Ould-Bouamama, B. (2006). Model based PEM fuel cell state-of-health monitoring via ac impedance measurements. *Journal of Power Sources*, 159(2), 905-913.

[22] He, W.S., Lin, G.Y., & Nguyen, T.V. (2003). Diagnostic tool to detect electrode flooding in proton-exchange-membrane fuel cells. *AIChE Journal*, 49(12), 3221-3228.

[23] Natarajan, D., & Nguyen, T.V. (2005). Current distribution in PEM fuel cells. Part 1: Oxygen and fuel flow rate effects. *AIChE Journal*, 51(9), 2587-2598.

[24] Kimball, E., Whitaker, T., Kevrekidis, Y., & Benziger, (2008). Drops, slugs, and flooding in polymer electrolyte membrane fuel cells. *AIChE Journal*, 54(5), 1313-1332.

[25] Hermann, H., Elsner, A., Hecker, M., & Stoyan, D. (2005). Computer simulated dense random packing models as approach to the structure of porous low-k dielectrics. *Microelectronic Engineering*, 81(2-4), 535–543.

[26] Scott, G.D., & Kilgour, D.M. (1969). The density of random close packing of spheres. *British Journal of Applied Physics*, 2(2), 863-866.

[27] Owe Berg, T.G., McDonald, R.L., & Trainor, Jr. R.J. (1969). Two-dimensional flow of spheres. *Powder Technology*, 3(1), 56-59.

[28] Powell, M.J. (1980). Computer-Simulated Random Packing of Spheres. *Powder Technology*, 25(1), 45-52.

[29] Jodrey, W.S., & Tory, E.M. (1985). Computer simulation of close random packing of equal spheres. *Physical Review A*, 32(4), 2347-2351.

[30] Nolan, G.T., & Kavanagh, P.E. (1992). Computer simulation of random packing of hard spheres. *Powder Technology*, 72 (2), 149–155.

[31] Adams, D.J., & Matheson, A.J. (1972). Computation of dense random packing of hard spheres. *The Journal of Chemical Physics*, 56(5) 1989-1994.

[32] Hermanna, H., Elsner, A., Lochmannb, K., & Stoyan, D. (2007). Optimisation of multicomponent hard sphere liquids with respect to dense packing. *Materials Science and Engineering: A*, 449–451, 666–670.

[33] George, J.A., & Robinson, D.F. (1980). A heuristic for packing boxes into a container. *Computers and Operations Research*, 7(3), 147-156.

[34] Thapatsuwan, P., Pongcharoen, P., Hicks, C., & Chainate, W. (2012). Development of a stochastic optimization tool for solving the multiple containers packing problems. *International Journal of Production Economics*, 140 (2) 737–748.

[35] Tulluri, S. (2003). *Analysis of random packing of uniform spheres*. Unpublished master thesis, New Jersey Institute of Technology, New Jersey, United State of America.

[36] Walthery, J.H., Jaffe, R., Haliciogluz, T., & Koumoutsakosy, P. (2000). Molecular dynamics simulations of carbon nanotubes in water. Center for Turbulence Research, Proceedings of the Summer Program.

[37] Girifalco, L.A., & Weizer, V.G. (1959). Application of the Morse Potential Function to Cubic Metals. *Physical Review*, 114(3), 687-690.

[38] Hamzacebi, C., & Kutay, F. (2007). Continuous functions minimization by dynamic random search technique. *Applied Mathematical Modelling*, 31(10), 2189–2198.

[39] Seidenberger, K., Wilhelm, F., Schmitt, T., Lehnert, W., & Scholta, J. (2011). Estimation of water distribution and degradation mechanisms in polymer electrolyte membrane fuel cell gas diffusion layers using a 3D Monte Carlo model. *Journal of Power Sources*, 196(12), 5317–5324.

[40] Seidenberger, K., Wilhelm, F., Haußmann, J., Markötter, H., Manke, I., & Scholta, J. (2013). Grand canonical Monte Carlo study on water agglomerations within a polymer electrolyte membrane fuel cell gas diffusion layer. *Journal of Power Sources*, 239, 628-641.

[41] Modak, A.U., & Lusk, M.T., (2005). Kinetic Monte Carlo simulation of a solid-oxide fuel cell:I. Open-circuit voltage and double layer structure. *Solid State Ionics*, 176(29-30), 2181 – 2191.

[42] Wang, X., Lau, K.C., Turner, C.H., & Dunlap, B.I. (2010). Kinetic Monte Carlo simulation of the elementary electrochemistry in a hydrogen-powered solid oxide fuel cell. *Journal of Power Sources*, 195(13), 4177–4184.

[43] Lau, K.C., Turner, C.H., & Dunlap, B.I. (2008). Kinetic Monte Carlo simulation of the Yttria Stabilized Zirconia (YSZ) fuel cell cathode. *Solid State Ionics*, 179(33-34), 1912–1920.

[44] Ge, X., Fu, C., & Chan, S.H. (2011). Double layer structure in solid oxide fuel cell anode/electrolyte interfaces: A Monte Carlo study. *Electrochemistry Communications*, 13(8), 792–795.

[45] Zhang, J., Yang, W., Xu, L., & Wang, Y. (2011). Simulation of the catalyst layer in PEMFC based on a novel two-phase lattice model. *Electrochimica Acta,* 56 (20), 6912– 6918.

[46] Suzuki, A., Sen, U., Hattori, T., Miura, R., Nagumoa, R., Tsuboi, H., … Miyamoto, A. (2011). Ionomer content in the catalyst layer of polymer electrolyte membrane fuel cell (PEMFC): Effects on diffusion and performance. *International Journal of Hydrogen Energy*, 36(3), 2221-2229.

[47] Bondi, A. (1964). van der Waals Volumes and Radii. *Journal of Physical Chemistry*, 68(3), 441–451.

[48] Choi, P., Jalani, N.H., & Datta, R., (2005). Thermodynamics and Proton Transport in Nafion II. Proton Diffusion Mechanisms and Conductivity. *Journal of the Electrochemical Society*, 152(3), E123-E130.

[49] Gertnera, B.J., & Hynes, J.T., (1998). Model molecular dynamics simulation of hydrochloric acid ionization at the surface of stratospheric ice. *Faraday Discuss.* 110, 301-322.

[50] Franks, F. (2000). *Water: A matrix of life* (2nd ed.). Royal Society of Chemistry: Cambridge.

[51] Cheng, X., Shi, Z., Glass, N., Zhang, L., Zhang, J., Song, D., … Shen, J. (2007). A review of PEM hydrogen fuel cell contamination: Impacts, mechanisms, and mitigation. *Journal of Power* Sources, 165(2), 739–756.

[52] Air Resource Laboratory: National Oceanic and Atmospheric Administration. (2008, September). *How much oxygen and carbon dioxide is there in the air we breath*?. Retrieve from http://www.arl.noaa.gov/faq_ac14.php

[53] Shi, Z., Song, D., Li, H., Fatih, K., Tang, Y., & Zhang, J. (2009). A general model for air side proton exchange membrane fuel cell contamination. *Journal of Power Sources*, 186(2), 435-445.

[54] Li, H., Zhang, J., Fatih, K., Wang, Z., Tang, Y., Shi, Z., … Joos, N. (2008). Polymer electrolyte membrane fuel cell contamination: Testing and diagnosis of toluene-induced cathode degradation. *Journal of Power Sources*, 185(1), 272–279.

[55] Li, H., Gazzarri, J., Tsay, K., Wu, S., Wang, H., Zhang, J., … Schrooten, J. (2010). PEM fuel cell cathode contamination in the presence of cobalt ion (Co^{2+}). *Electrochimica Acta*, 55(20), 5823–5830.

[56] Sun, M., Song, W., Zhai, L., & Tong, Z. (2014). Iron-contamination-induced performance degradation of an iron-fed fuel cell. *Journal of Power Sources*, 248(15), 6-14.

[57] Bouzek, K., Paidar, M., Maliˇs, J., Jakubec, I., & Janík, L. (2010). Influence of hydrogen contamination by mercury on the lifetime of the PEM-type fuel cell. *Electrochimica Acta*, 56(2), 889–895.

[58] Mohtadi, R., Lee, W-K., & van Zee, JW. (2004). Assessing durability of cathodes exposed to common air impurities. *Journal of Power Sources*, 138(1-2), 216-225.

[59] Sulek, M., Adams, J., Kaberline, S., Ricketts, M., & Waldecker, J.R. (2011). In situ metal ion contamination and the effects on proton exchange membrane fuel cell performance. *Journal of Power Sources*, 196(21), 8967– 8972.

[60] Yang, D., Ma, J., Xu, L., Wu, M., & Wang, H. (2006). The effect of nitrogen oxides in air on the performance of proton exchange membrane fuel cell. *Electrochimica Acta*, 51(19), 4039-4044.

[61] Chu, H.S., Wang, C.P., Liao, W.C., & Yan, W.M. (2006). Transient behavior of CO poisoning of the anode catalyst layer of a PEM fuel cell. *Journal of Power Sources*, 159(2), 1071-1077.

[62] Los Alamos National Laboratory. (2013, December). *Periodic Table of Elements: iron*. Retrieve from http://periodic.lanl.gov/26.shtml

[63] Los Alamos National Laboratory. (2013, December). *Periodic Table of Elements: aluminum*. Retrieve from http://periodic.lanl.gov/13.shtml

[64] Halicioglu, T., & Pound, G.M. (1975). Calculation of Potential Energy Parameters. *Physica Status Solidi (a)*, 30(2), 619-623.

[65] National Oceanic and Atmospheric Administration (2013, December). *Up-to-date weekly average CO_2 at Mauna Loa*. Retrieve from http://www.esrl.noaa.gov/ gmd/ccgg/trends/weekly.html

[66] Gosink, T. (1983). *What Do Carbon Monoxide Levels Mean?*. Retrieve from Alaska Science Forum, Geophysical Institute, University of Alaska Fairbanks website: http://www2.gi.alaska.edu/ScienceForum/ASF5/588.html

[67] Haynes, W.M. (2010). *Handbook of Chemistry and Physics* (91st ed.). Boca Raton,

Florida: CRC Press.

VITA

Graduate College

University of Nevada, Las Vegas

Karn Soontrapa

Address:

1401 Elizabeth Ave Unit 1 Las Vegas, Nevada 89119

Degrees:

Master of Engineering, Industrial Engineering, 2007

Chulalongkorn University, Bangkok, Thailand

Bachelor of Science, Physics, 2004

Chulalongkorn University, Bangkok, Thailand

Experience:

2009 to 2010: Operation Analyst / Operation manager, Ceva Logistics (Thailand)

2007 to 2008: Engineer, Toyota Motor (Thailand)

Publication:

Soontrapa, K., & Chen, Y. (2013). Mono-sized sphere packing algorithm development using optimized Monte Carlo technique. *Advanced Powder Technology*, 24(6), 955–961.

Soontrapa, K., & Chen, Y. (2013). Development of computational geometry
    algorithm for water distribution in PEMFC's cathode catalyst layer using
    Monte Carlo technique. *Journal of Power Sources*, (Submitted, in review
    process).

Soontrapa, K., & Chen, Y. (2013). Determination of the metal impurity and gases
    contamination effect on the performance of PEMFC using Monte Carlo
    computational geometry algorithm. *Journal of Power Sources*, (Submitted, in
    review process).

Dissertation Title: Study of water transport phenomena on cathode pf PEMFCS using
Monte Carlo simulation

Dissertation Examination Committee:

Chairperson, Yitung Chen, Ph. D.

Committee Member, Robert Boehm, Ph. D.

Committee Member, William Culbreth, Ph. D.

Committee Member, Mohamed Trabia, Ph. D.

Graduate Faculty Representative, Jichun Li, Ph. D.